The Pennsylvania State University

The Graduate School

College of Engineering

CHARACTERISTIC BEHAVIOR OF POLYMER ELECTROLYTE FUEL CELLS DURING COLD START

A Thesis in

Mechanical Engineering

by

Charles Chacko

Submitted in Partial Fulfillment

of the Requirements

for the Degree of

Master of Science

August 2008

The thesis of Charles Chacko was reviewed and approved* by the following:

Matthew M. Mench

Associate Professor of Mechanical Engineering

Thesis Advisor

Kendra V. Sharp

Assistant Professor of Mechanical Engineering

Karen A. Thole

Professor of Mechanical Engineering

Head of the Department of Mechanical and Nuclear Engineering

*Signatures are on file in the Graduate School

Abstract

In this study, experimental constant-current cold starts were performed on a polymer electrolyte fuel cell (PEFC) from -10°C in order to characterize high frequency resistance behavior (HFR), water motion, and ice accumulation before, during, and after cold start. A new diagnostic method for rapid and repeatable cold starts was developed and verified. HFR is shown to be a key diagnostic for cold start behavior and performance. Cold start performance, as measured by the amount of water produced during the cold start, is found to be optimized when cell resistance is increasing prior to startup, which is indicative of polymer electrolyte membrane (PEM) dehydration. During cold start, cell resistance initially decreases due to PEM hydration by the product water. Interestingly, after a certain water uptake capacity of the PEM is reached, resistance increases due to ice formation in and around the cathode catalyst layer (CL) with evidence of super-cooled water flow at low currents. Utilizing lower startup currents apparently does not increase the PEM water storage capability, but does increase the total volume of ice in and around the CL before freeze-out. Lower startup currents were found to produce more total heat, but at a reduced rate compared to high current densities. Therefore, an acceptable current density range exists for a given stack design which ensures sufficient heat is produced to raise cell temperature above 0°C before freezing out occurs, which is the overall design goal.

Table of Contents

List of Figures

List of Tables

Nomenclature

Acronyms

AC	Alternating current
CL	Catalyst layer
DC	Direct current
DM	Diffusion media
EIS	Electrochemical impedance spectra
FCDDL	Fuel Cell Dynamics and Diagnostics Laboratory
GDL	Gas diffusion layer
HFR	High frequency resistance
ICE	Internal combustion engine
MEA	Membrane electrode assembly
MPL	Microporous layer
NASA	National Aeronautics and Space Administration
OCV	Open circuit voltage
PEFC	Polymer electrolyte fuel cell
PEM	Polymer electrolyte membrane
PTFE	Polytetrafluoroethylene
RH	Relative humidity

Parameters

A	cross-sectional area, m^2
a	water activity
D	diffusion of water into membrane, m^2/sec
E	energy, J
E_{th}	thermal potential, V
$\dot{E}$	energy generation rate, J/sec
EW	equivalent weight, kg/mol
F	Faraday's constant, 96,487 C/mol-eq
i	current density, A/m^2
m	mass of water, kg
M_{H_2O}	molecular weight of water, 0.018 kg/mol
$\dot{n}$	molar flow rate, mol/sec
P	pressure, atm
Q	heat, J
$\dot{Q}$	heat generation rate, J/sec
R'	resistance change over time, $\Omega\ m^2$/sec
t	time, sec
T	temperature, K

Subscript

a	anode
act	actual
avg	average
c	cathode
cell	cell
CL	catalyst layer
dehyd	dehydration
diff	diffusion
dry	dry
i	initial
PEM	polymer electrolyte membrane
pro	produced
rem	removed
sat	saturation
sto	stored
SU	startup

Greek

Δ	change
δ	thickness, m
ε	porosity
$\varepsilon_{CL,e}$	volume fraction of ionomer in CL
λ	membrane water content, # H_2O / SO_3^-
ρ	density, kg/m^3
σ	membrane conductivity, S/m
τ	diffusion time coefficient, sec

Acknowledgments

I would first and foremost like to thank my thesis adviser, Dr. Matthew M. Mench, director of the Penn State Fuel Cell Dynamics and Diagnostics Laboratory (FCDDL). His continuous guidance and support throughout my graduate studies helped me press on and perform at my best. I could not have chosen a better research adviser and I wish him a very fruitful life and career.

I would also like to thank my fellow lab mates in the Penn State FCDDL for their advice, help, and friendship. To Dr. Ramaraja Ramasamy, thank you for all of your assistance in the laboratory – I could not have completed this work without your help. To Mr. Soowhan Kim, thank you for all of your technical advice and guidance. To Mr. Manish Khandelwal, thank you for your insight involving not only research, but life in general. I wish the entire FCDDL all the best success in life.

I could not have completed my graduate studies without the love and support of my family. To my mother, thank you for keeping calm and level-headed throughout all of my schooling. To my father, thank you for all of your encouragement, advice, and support throughout my undergraduate and graduate years. Jules, I am very grateful for all you have done for me while being so understanding, cooperative, and patient. To the Kaplows, thank you for your hospitality and warmth over the past two years. I love all of you very much.

Chapter 1 Introduction

1.1 Background

A fuel cell is a device that converts the chemical energy stored in a fuel and oxidizer directly into electrical energy. This electrical energy can be used to power nearly anything, ranging from notebook computers to automobiles to entire cities. In general, a fuel cell consists of two electrodes separated by an electrolyte. Fuel is supplied to one electrode, the anode, while oxidizer is supplied to the other, the cathode. The electrolyte separator enables a voltage difference between the fuel and oxidizer, and by electrochemical reactions at the electrode surfaces, an electric current can be drawn from the fuel cell.

The history of fuel cells dates back to 1839, when Sir William Grove reversed the process of electrolysis by combining hydrogen and oxygen to create water and generate an electric current. This process required the use of platinum electrodes submerged in an electrolytic sulfuric acid solution. However, due to limitations associated with the catalyst and the cell's power density, it was not until the 1950s when fuel cells were used in a practical application. In 1955, William Grubb of General Electric developed a low-temperature polymer electrolyte fuel cell (PEFC) to be used in the NASA Gemini space program. NASA has also developed fuels cell using an alkaline electrolyte solution for their Apollo space program. In fact, alkaline fuel cells still serve as auxiliary power units for the Space Shuttle orbiter [1].

The electrolyte material is a key component of a fuel cell, and must possess certain attributes, most important of which is being an ionic conductor and electrical insulator. Since the formative years of fuel cells, various types of electrolytes have been employed, each having its own advantages and disadvantages. Consequently, a fuel cell is categorized by the type of electrolyte it utilizes [2].

One of the major advantages of a fuel cell is the potential for high efficiency operation. Because of this, a highly anticipated goal of the fuel cell is to replace modern heat engines, such as internal combustion engines (ICEs) and gas turbines. Unlike heat engines, fuel cells are not limited by the Carnot cycle and can theoretically reach efficiencies above 90%. As a comparison, a practical heat engine can achieve a Carnot efficiency of about 45% [2]. Even when taking entire system losses and cogeneration into account, a fuel cell can achieve an overall efficiency of 50-80% while the heat engine can reach an overall efficiency of 15-45%, as shown in Figure 1.1 [3].

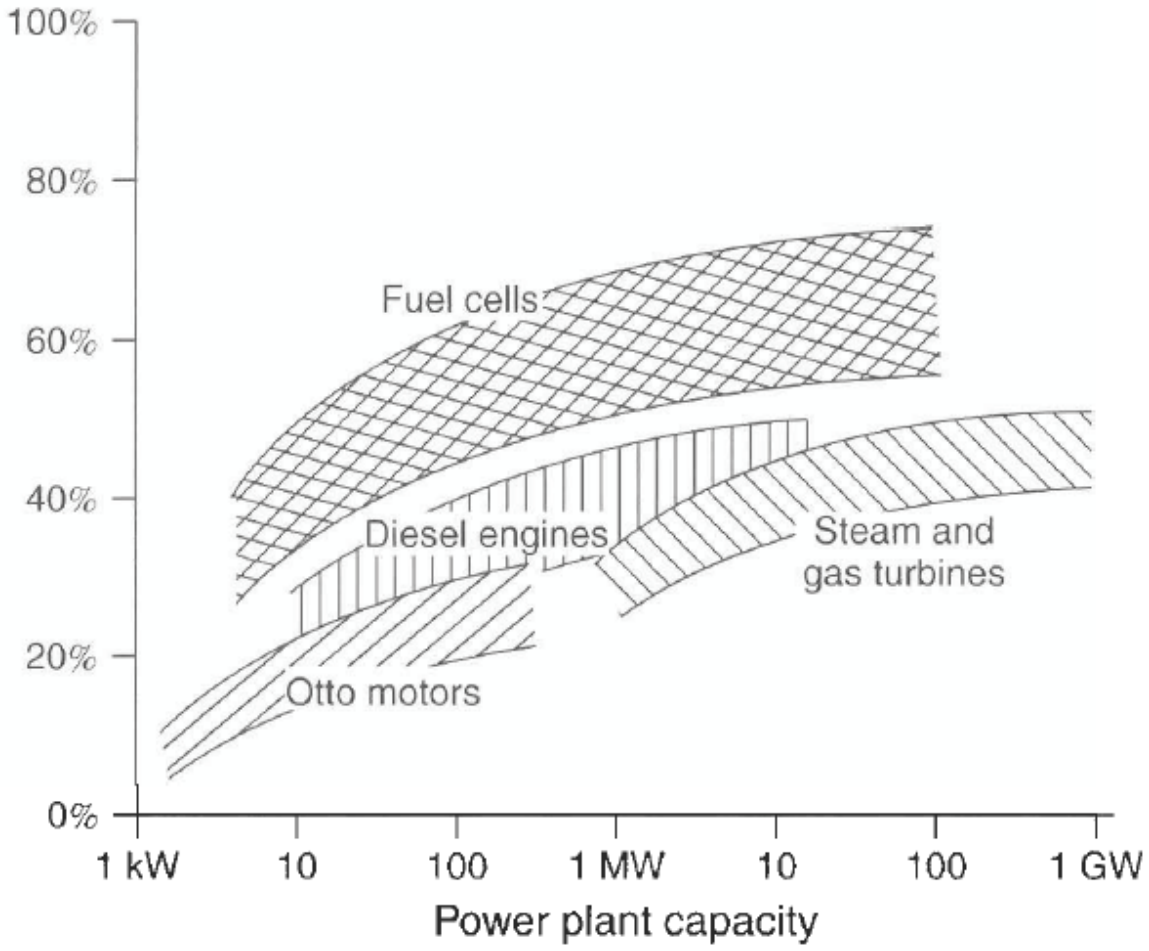

Figure 1.1 - Typical efficiencies of various energy conversion systems as a function of power output [3].

In addition, a fuel cell running on pure hydrogen produces ultra-low to zero emissions, except those associated with the production of hydrogen itself. For example, a typical PEFC electrochemical reaction is given by:

$$\begin{aligned} &\text{Anode:} && 2H_2 \rightarrow 4H^+ + 4e^- \\ &\text{Cathode:} && 4H^+ + 4e^- + O_2 \rightarrow 2H_2O \\ &\text{Overall:} && 2H_2 + O_2 \rightarrow 2H_2O \end{aligned} \tag{1.1}$$

While electricity is generated as the product of a PEFC, the only byproducts are water and heat; no greenhouse gases or pollutants are produced (except for emissions associated with fuel production). Also, if the hydrogen is derived by electrolysis or from biomass, and oxygen is taken directly the atmosphere, the fuel cell is able to run on a renewable energy source.

Another advantage of fuel cells is their quiet and low temperature operation. The only moving parts in a fuel cell system are the pumps and blowers feeding fuel and oxidizer into the system. This greatly reduces the noise produced during operation in comparison to most conventional engines. Typical PEFC operating temperatures can range from 100°C down to room temperature, enabling them to have a small thermal signature which can be beneficial for many military applications [1]. Another benefit of utilizing fuel cells is modularity; an array of fuel cells, called a fuel cell stack, can increase its power output simply by adding cells or geometrically scaling up the cells within the stack.

As the world is continually trying to improve on energy efficiency, fuel cells have the opportunity to prove themselves an optimal energy conversion device. A key topic of interest is the use of fuel cells as primary engines for automobiles. One of the most promising types fuel cells for automotive applications, among other types of portable power, is the PEFC due to its relatively small size and low operating temperatures [1]. The focal point of research in this study is the PEFC; therefore subsequent sections will focus specifically on this type of fuel cell.

1.2 Polymer Electrolyte Fuel Cell

1.2.1 Description

The PEFC electrochemical reaction is given in Eq. 1.1. The reaction begins when the fuel, hydrogen, and oxidizer, oxygen, is supplied to the anode and cathode side of the PEFC, respectively. The difference in electrical potential between the fuel and oxidizer creates a direct-current (DC) voltage difference. As hydrogen comes into contact with a platinum catalyst layer, electrons are removed from the hydrogen atoms. The electrically insulating polymer electrolyte forces the electrons to flow through an external circuit, creating a DC current which draws energy from the fuel cell. The resulting positively charged hydrogen ion, H^+, is passed through the ion-conducting electrolyte membrane and meets with oxygen on the cathode electrode of the PEFC. The hydrogen and oxygen then combine with electrons to create water and exit through the exhaust of the fuel cell.

A schematic of a PEFC can be seen in Figure 1.2. In the center of the fuel cell is the polymer electrolyte membrane (PEM). The main roles of the membrane are to allow H^+ ions to pass from the anode to the cathode, insulate electron transport through the fuel cell, and physically separate the fuel and oxidizer [1]. The most common type of membrane used in PEFCs is a polymer perfluorosulfonic acid-polytetrafluoroethylene (PTFE) copolymer in acid. A common type of this membrane used is DuPont's Nafion®, typically ranging from 18-175 μm in thickness.

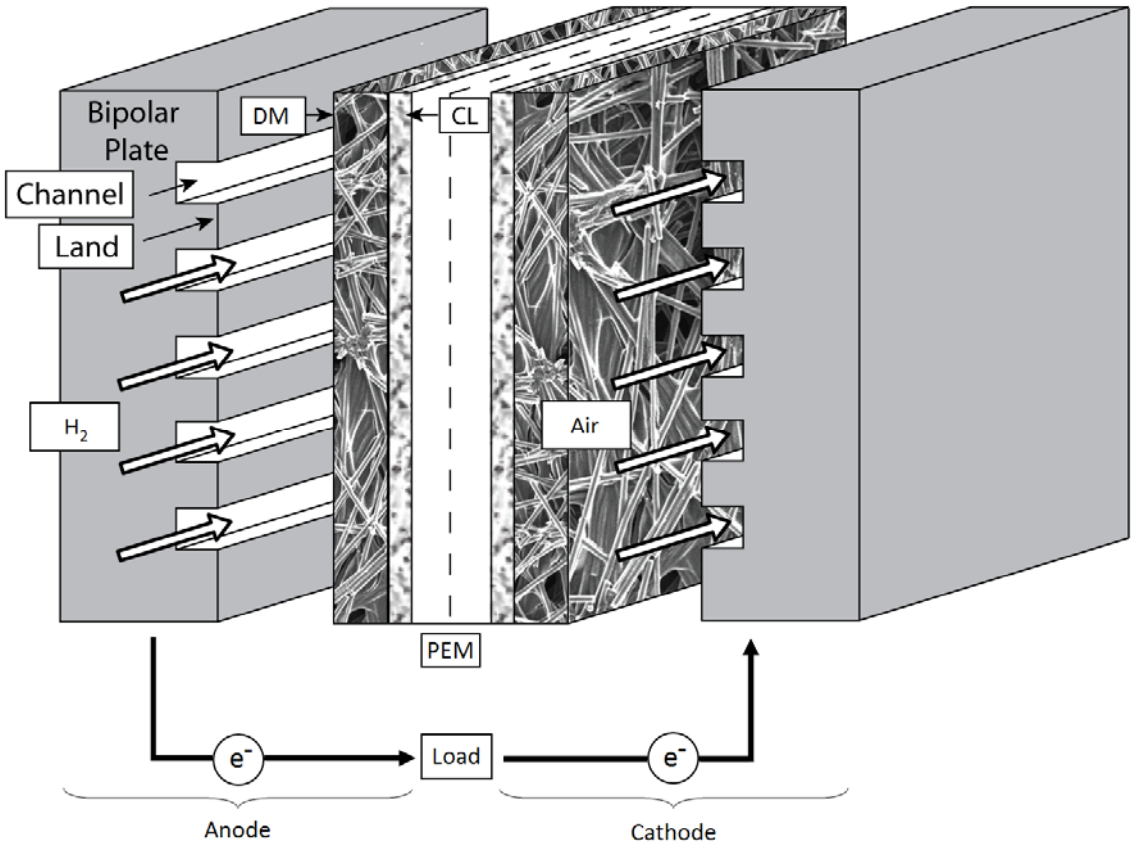

Figure 1.2 - Schematic of a polymer electrolyte fuel cell [1].

The ionic conductivity, σ, of the membrane is a strong function of its water content, λ, and temperature [4]. The membrane water content is quantified by the ratio of molecules of water attached to the number of charge sites in the membrane. Membrane water content can be related to water activity surrounding the membrane, a, by the Springer relationship given as [5]:

$$\lambda = 0.043 + 17.81a - 39.85a^2 + 36.0a^3 \tag{1.2}$$

During fuel cell operation, the water activity is equal to the water saturation level of the membrane which is controlled by the relative humidity, RH, of the gas flowing through

the cell. The ionic conductivity of Nafion® membranes can then be related to λ and the temperature of the cell and membrane, T_{cell}, by a relationship such as [5]:

$$\sigma = \exp\left[1268\left(\frac{1}{303} - \frac{1}{T_{cell}}\right)\right] \cdot (0.005139\lambda - 0.00326) \tag{1.3}$$

On both sides of the membrane are the fuel cell electrodes, or catalyst layers (CLs). The chief roles of the CLs are to serve as reaction sites and provide a flow path for electrons. This dual responsibility requires the CLs to have a unique structure. Typically the CLs consist of a fine powder of 5μm carbon particles coated in smaller 2 nm platinum particles. The carbon serves as an electronic conductor while the platinum acts to lower the activation energy of the electrochemical reactions. This powder gives the CLs a porous structure, approximately 60% porous, and gives the reactant gases greater surface area exposure to the platinum, allowing for maximum utilization of fuel and oxidizer. This 10-50 μm thick powder is typically hot pressed directly onto the membrane as an ink or slurry, creating a membrane electrode assembly, or MEA [2].

The diffusion media (DM), or gas diffusion layers (GDL), are positioned between the CL and gas flow channels. The DM essentially serve five purposes: transporting reactant gases to the CL, removing product water from the CL, transporting electrons from the CL, providing proper thermal management for the CL, and providing structural support for the MEA. The DM is typically a carbon cloth or carbon paper and much more robust than the MEA, ranging 200-420 μm in thickness. The structure of the DM allows it to be more porous than the CL, with pore sizes of approximately 10-30 μm and porosity around 80%. Furthermore, a thin micro-porous layer (MPL) may be added to the CL-side of the DM to provide better water management. The MPL is typically 30-50

μm thick with pore sizes on the order of 100-500 nm. The MPL acts to remove water from the MEA when the reaction site becomes over-saturated and also contain water within the MEA when it is under-saturated. A common DM/MPL used in PEFC applications is a carbon fiber paper made by Sigracet®, such as SGL10BB [6].

The flow channels, which typically are machined into the bipolar plates, are directly adjacent to the DM. The flow channels are responsible for supplying reactant gas into the fuel cell while the bipolar plates conduct electrons from the fuel cell to the external circuit. The bipolar plates also serve to add physical strength to the fuel cell structure and must be corrosion resistant due to the oxidizing and reducing environments to which they are exposed. Most bipolar plates also contain coolant channels to provide proper thermal management. Therefore these plates must be thermally as well as electronically conductive. A type of material that meets these requirements and is typically used is graphite and its alloys [6].

1.2.2 Polarization Curve

The performance of a fuel cell can be described by its polarization curve. A typical PEFC polarization curve can be seen in Figure 1.3. The polarization curve is a measurement of how much current can be drawn from a PEFC at a given voltage. To compare fuel cells of different sizes, the polarization curve is normalized by dividing the current drawn from the cell by the active area of the CL, this value being termed current density, i. The voltage of the cell that is obtained when no current is being drawn is referred to as open circuit voltage, or OCV. In general, the voltage difference the cell can

maintain decreases as more current is drawn. This voltage loss is the result of various inefficiencies and resistances associated with the fuel cell.

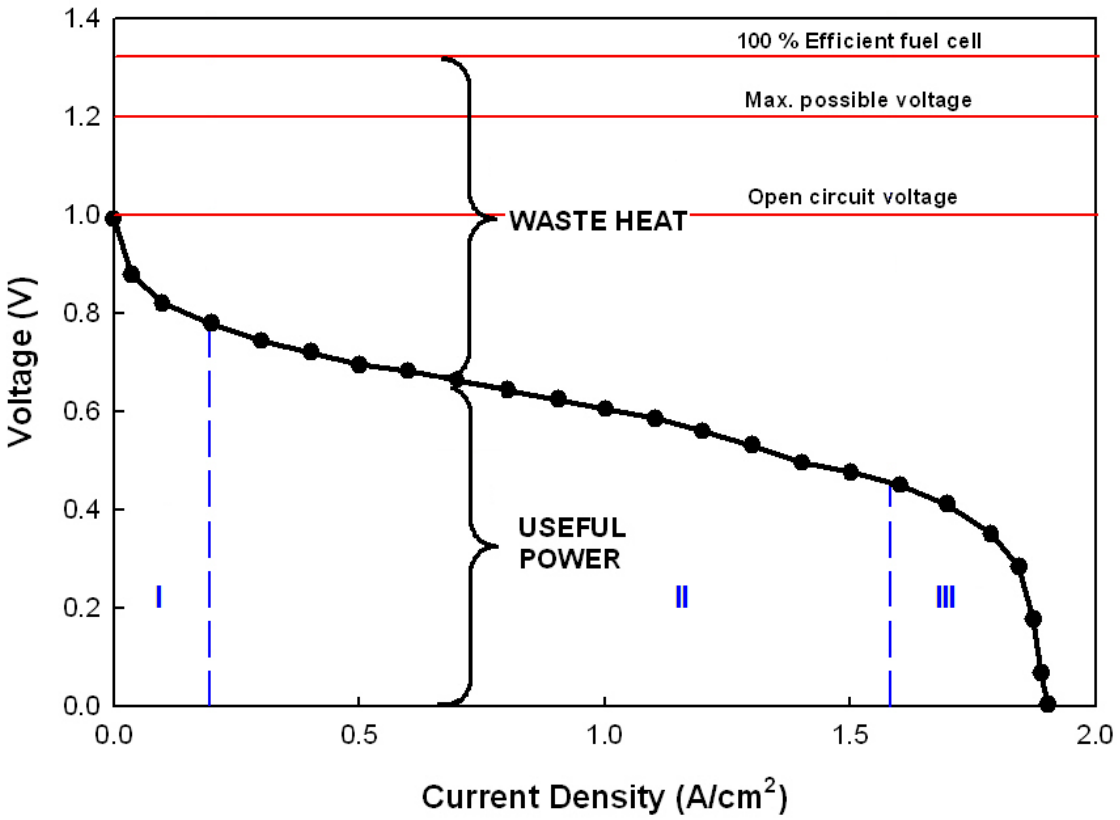

Figure 1.3 - Typical polymer electrolyte fuel cell polarization curve.

The polarization curve can be divided into three separate regions where specific losses dominate: (I) activation, (II) ohmic, and (III) mass transport. These regions are fully described in [1], but a brief description proceeds. Activation losses result from additional energy being required to raise the actual reaction rate to what is currently being demanded of the fuel cell [1].

Ohmic polarization losses are a direct result of Ohm's law, $V = IR$, and resistances are attributed to the resistivity of the different fuel cell components. Typically, the membrane can be responsible for a considerable amount of these losses. As shown in Eq. 1.2, membrane conductivity is a strong function of its water content and temperature; if a membrane is not fully saturated and/or at low temperature, it may account for significant ohmic losses [1].

As the cell is operated at higher current densities, the CLs require a greater supply of reactant gas in order to increase the electrochemical reaction rate. Sufficiently transporting these reactants to the CL surfaces prove challenging, especially at the cathode due to product water blocking reaction sites, this phenomenon is termed flooding. As the reaction sites are starved of reactants, the amount of current that can be drawn from the cell quickly diminishes to zero [1].

There are several diagnostic methods that can be used to quantify the three different types of resistances that cause the polarization losses associated with fuel cell operation. A common technique used to quantify the ohmic resistance of the fuel cell (Region II in Figure 1.3) is high frequency resistance, or HFR. HFR is a key diagnostic tool used in this study, and is subsequently discussed [1].

To first explain the principle of HFR, it should be noted that a fuel cell can be electronically modeled as a Randles circuit, sketched in Figure 1.4. Each circuit element represents a specific component or electrochemical process in the fuel cell. The voltage source is the DC voltage produced by the fuel cell. The polarization resistor represents the charge transfer resistance while the electrolyte resistor represents the ohmic resistance

(Regions I and II in Figure 1.3, respectively). The capacitor represents the interfacial capacitance of the CL [7].

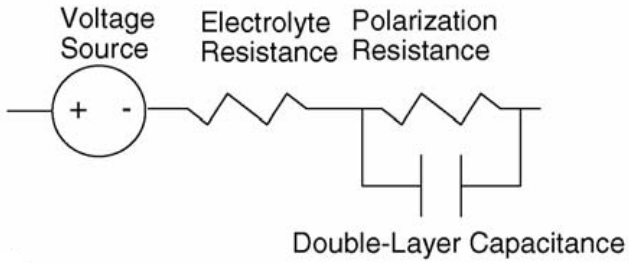

Figure 1.4 - Equivalent circuit of catalyst layer [7].

Under normal low-current operation, shown in Regions I and II Figure 1.3, the cell resistance that can be obtained from Ohm's law primarily represents both the ohmic and charge transfer resistance. In order to distinguish between these two, HFR can be utilized, which is schematically shown in Figure 1.5. To measure HFR, a small alternating-current (AC) signal is applied to the cell (typically less than 5mA of frequency on the order of 1 kHz) which modulates the electronic load from the test station. At this high frequency, the capacitor shown in Figure 1.4 behaves as a short circuit, resulting in the electrical bypass of the polarization resistor. The frequency response analyzer then measures the response of the AC voltage and current of the cell and determines the cell impedance. Because the polarization resistor is bypassed, this impedance is a direct measurement of the ohmic resistance of the fuel cell [7]. This ohmic resistance includes both the ohmic resistance of the membrane as well as the contact resistances present throughout the fuel cell. In general, an HFR measurement

lasts a short duration, usually on the order of 1 ms, and minimally disturbs the cell, making it a suitable during normal operation.

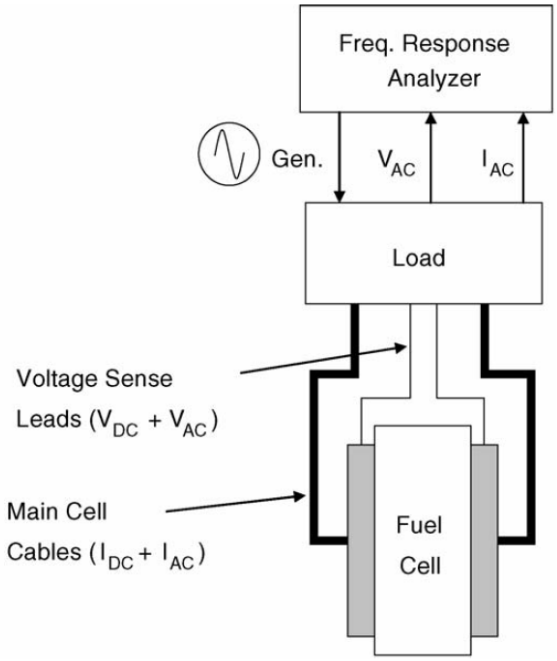

Figure 1.5 - Schematic of equipment set-up for high frequency resistance [7].

1.2.3 Problem Overview

Since water is a product of the fuel cell reaction, operating the PEFC below freezing temperatures is challenging; water produced by the electrochemical reaction can quickly solidify into ice, blocking the reaction sites of the CL, and terminating the reaction (a freeze-out). Cell startup from a frozen condition, or cold start, is a recent topic of interest. When a freeze-out occurs during cold start, no energy can be drawn from the cell, in effect rendering the cell useless. In addition, the formation of ice during cold start may accelerate local catalyst and material degradation.

Of course, the cell can be heated by external means, but this requires additional energy, ultimately leading to a sacrifice in system efficiency. In an ideal scenario, the heat generated by the electrochemical reaction would raise the cell temperature above 0°C before freeze-out occurs anywhere in the cell or stack, allowing a damage free self-start.

1.3 Literature Review

During cold start, cell performance further suffers due to sluggish kinetics as well as low membrane conductivity associated with low temperatures [5,8-11]. Cappadonia *et al.* [11] showed that conductivity vs. temperature (σ vs. T) plots of water-saturated Nafion® membranes revealed a significant decrease in σ at 0°C, indicating a phase change of water. For fully-saturated Gore™ membranes, Tajiri *et al.* [10] attributed this decrease in conductivity to residual water diffusing out of the membrane during cool down, freezing, and increasing contact resistance between fuel cell components, which is also consistent with the view of He and Mench [12-14].

The most basic way of analyzing cold start performance is describing the cold start as a success (self-start) or a failure (freeze-out). A self-start occurs when the heat generated by the electrochemical reaction raises the cell temperature above 0°C before the generated water has a chance to freeze and cover the reaction sites of the CL. A freeze-out occurs when ice covers these reaction sites and the electrochemical reaction is terminated. One way to quantify cold start performance, regardless of self-start or freeze-

out, for a single fuel cell in an isothermal environment is the amount of water produced, m_{pro} , before a freeze-out occurs:

$$m_{pro} = A\frac{M_{H_2O}}{2F}\int_{t=0}^{t=freeze-out} i\,dt \tag{1.4}$$

where A is the active area of the fuel cell, M_{H_2O} is the molecular weight of water, F is Faraday's constant, t is the time from the beginning of startup until freeze-out, and i is the startup current density. Many key parameters that affect cold start performance have been identified in the literature, including membrane water content, startup current density, reactant gas flow rates, and the phase of product water.

It has been found that a dry membrane state prior to cold start is beneficial for performance, since it increases the membrane water storage capacity [10,15-19]. During cold start, the membrane absorbs some of the product water, prolonging the time until freeze-out occurs. As shown in Figure 1.6 [10], as membrane water uptake potential increases (i.e. the membrane is drier prior to startup), the amount of water that is produced during cold start increases.

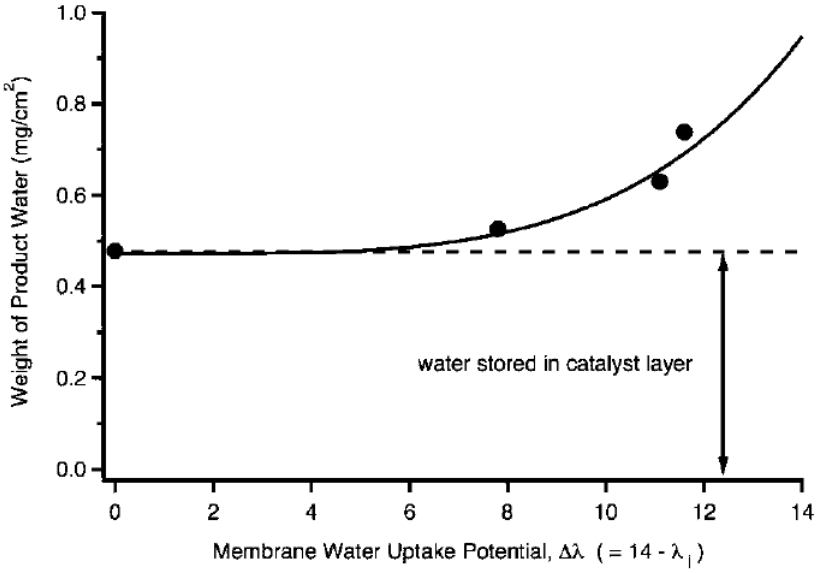

Figure 1.6 - Relation between product water and membrane water uptake potential for cold start from -30°C. The dashed line indicates the amount of water stored in the catalyst layer and the extra portion above it denotes the amount of water diffused into the membrane [10].

Directly related to membrane water content, the shutdown purge procedure has been shown to play a significant role, as a dryer membrane results in increased cold start performance [17,20] as well as an increased chance of self-start [21,22]. Furthermore, a shutdown purge that removes residual water in the CL has been shown to eliminate freeze/thaw cycle damage [12-14,23,24]. Figure 1.7 is a scanning electron microscope image which shows how ice formation between the membrane and CL can cause the CL to separate or delaminate from the membrane [24]. This delamination can significantly reduce PEFC performance.

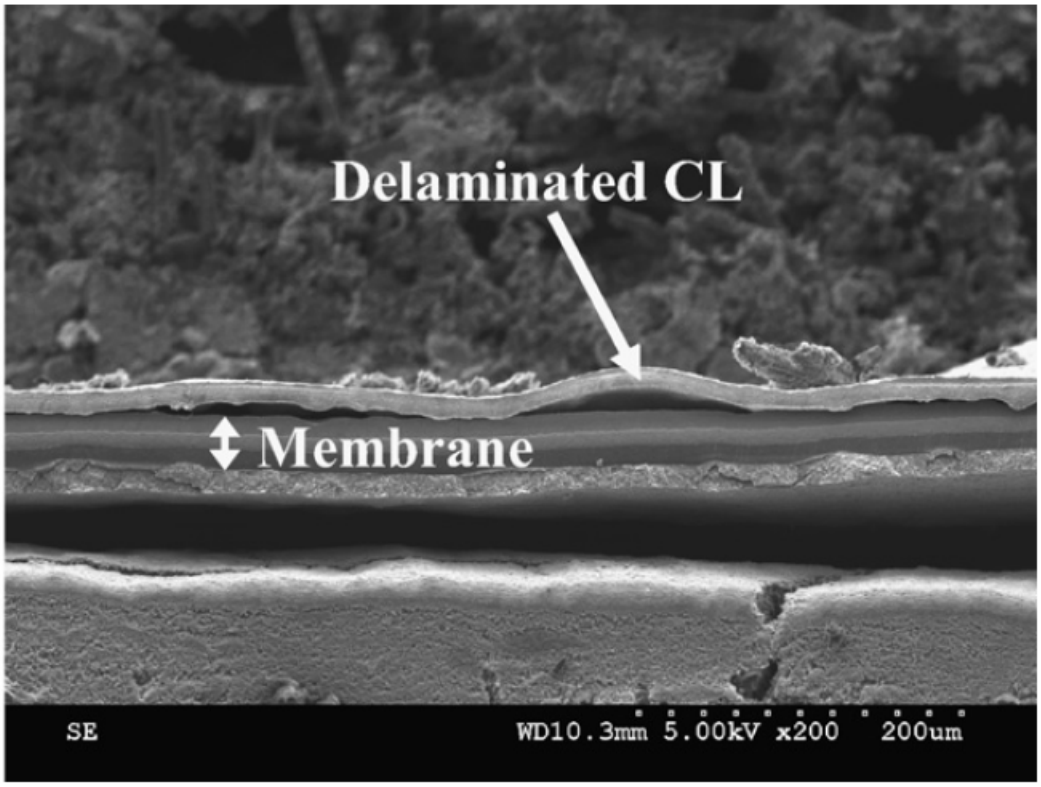

Figure 1.7 - Cross-sectional scanning electron microscope image of MEA that was freeze/thaw cycled 30 times under fully humidified conditions [24].

Utilizing a lower startup current density has also been shown to improve cold start performance in various publications [10,17,19,25]. Specifically, Mao *et al.* [19] sited that lower current densities enable more water to be absorbed into a dry membrane. As sketched in Figure 1.8 Tajiri *et al.* [10] explained that higher current densities may form a premature ice layer between the CL and DM (labeled GDL here) and cover reaction sites; hence the CL pore space is not fully utilized for water storage.

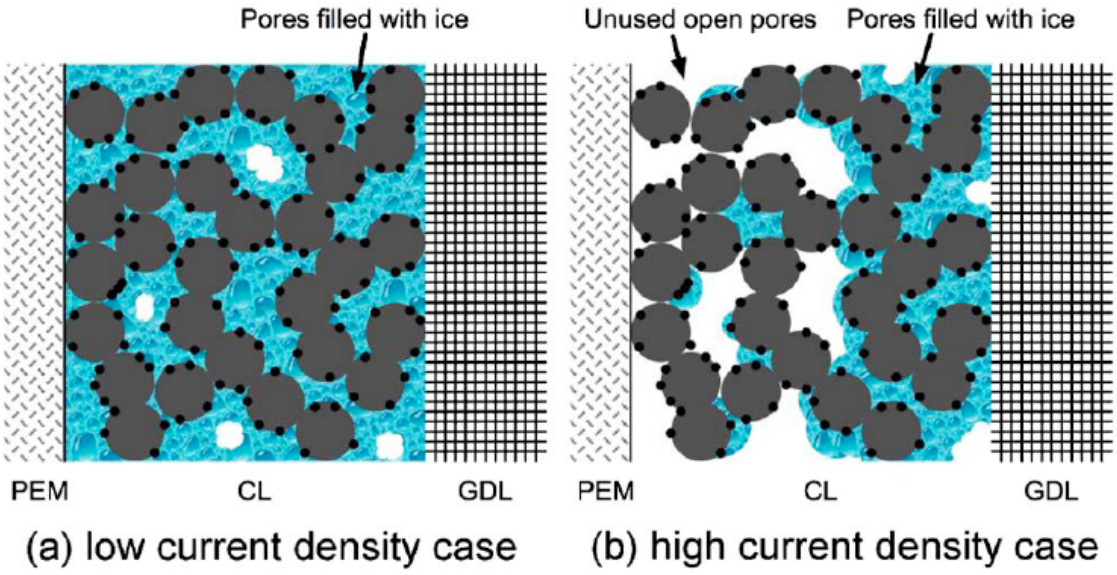

Figure 1.8 - Schematic of water distribution at the end of cold start for (a) low current density, and (b) high current density [10].

During startup, water removal by the reactant gas flow can impact performance as well. Oszcipok *et al.* [15,16] determined by statistical analysis that cathode air flow rate significantly affects cold start performance. It was also demonstrated by Causey *et al.* [22] that doubling the air flow rate alone can result in self-start as opposed to freeze-out, indicating that water removal in the vapor phase can play a significant role during cold start.

Several in situ imaging studies were performed to determine the phase of product water during cold start. Ishikawa *et al.* [26,27] showed that liquid water can exist on the cathode CL in a super-cooled state at -10°C. However Ge *et al.* [20,28] stated that liquid water cannot exist on the cathode CL below -1.5°C.

The behavior of various fuel cell resistances has been studied in literature as well. Oszcipok *et al.* measured the electrochemical impedance spectra (EIS) during cold start

and determined that HFR decreases due to membrane hydration while charge transfer resistance significantly increases due to ice coverage of the reaction surfaces [15]. This is shown in Figure 1.9, where HFR is denoted as $R_{m,c}$ and charge transfer resistance is denoted as R_{ct}. The x-axis in Figure 1.9 is the cumulated charge transfer density, which is linearly related to the amount of water produced during cold start. Figure 1.10 highlights the findings of Tajiri *et al.*, who also concluded that HFR decreases during cold start due to membrane hydration [10]. In a later study, Oszcipok *et al.* [29] observed that during cold start, HFR initially decreased, but exhibited a noticeable step increase. This step can be seen in the -8°C case shown in Figure 1.11. This step was attributed to an increase in contact resistance due to ice formation.

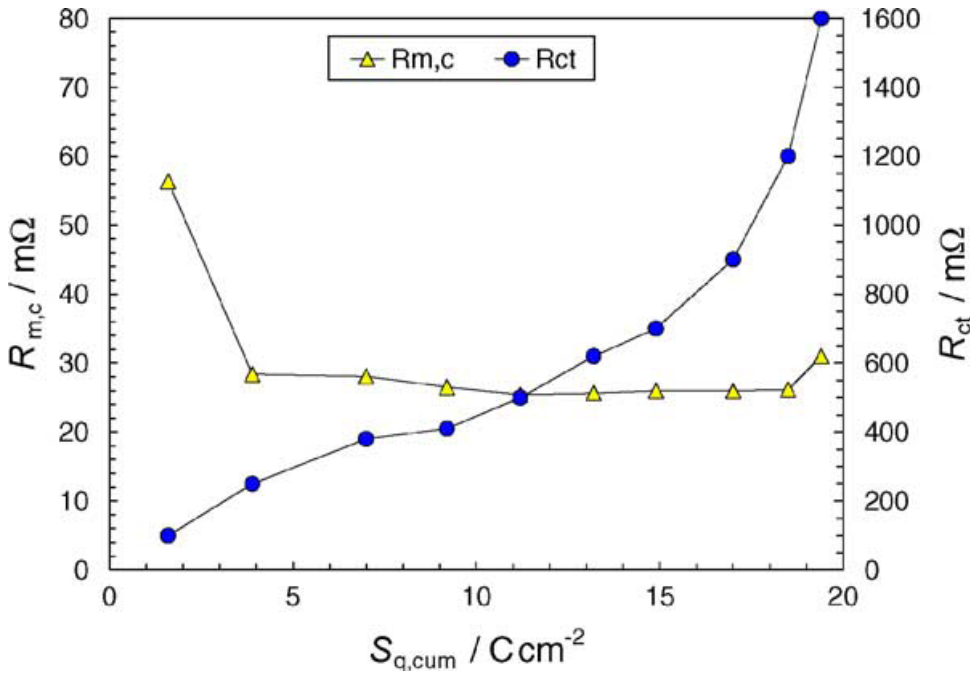

Figure 1.9 - Membrane/contact resistance, R_{mc} (HFR), and charge transfer resistance, R_{ct}, as a function of cumulated charge transfer density [15].

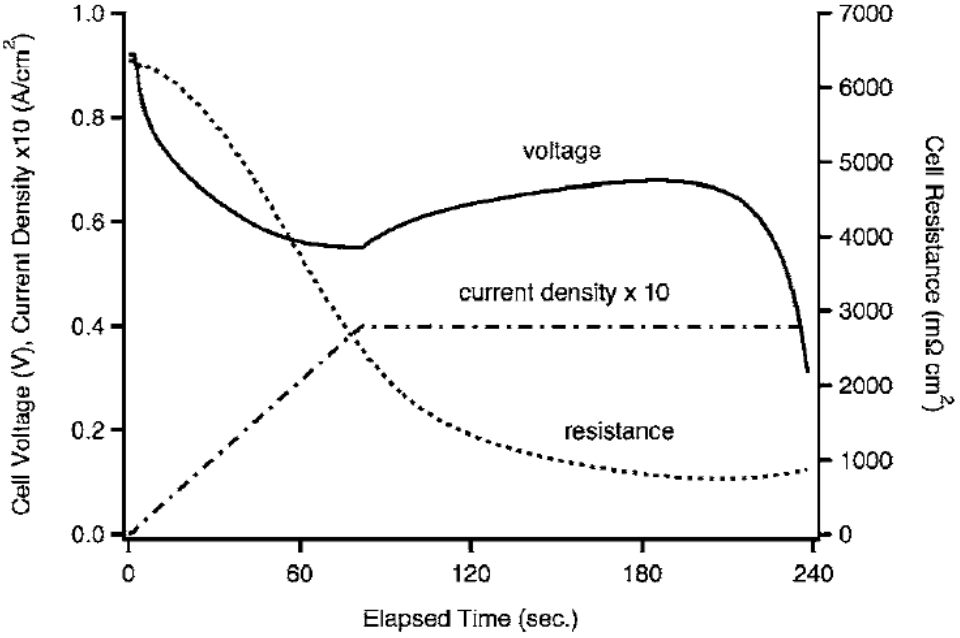

Figure 1.10 - Time evolution of applied current density, cell voltage, and cell resistance (HFR) during cold start [10].

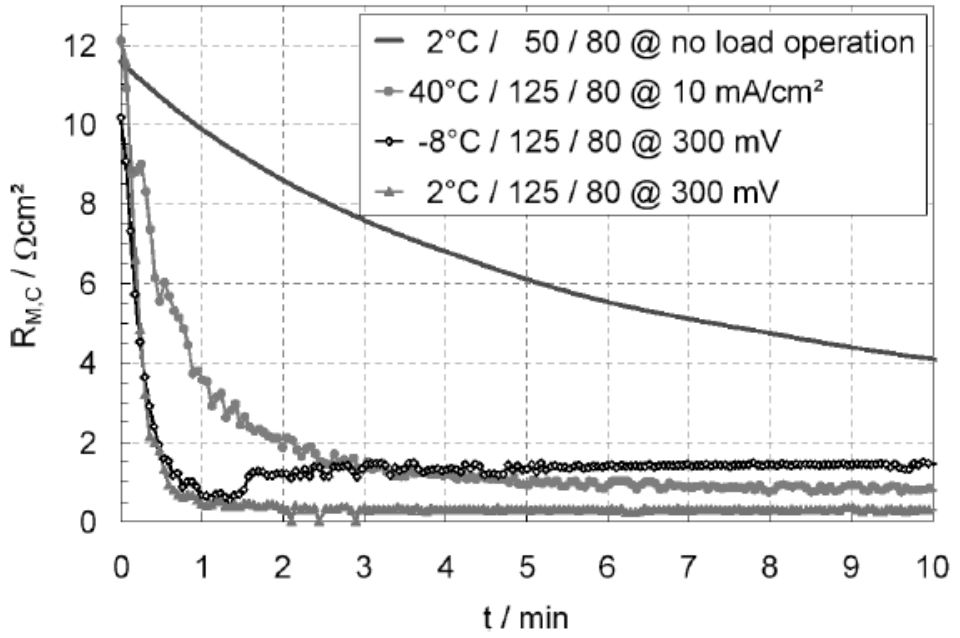

Figure 1.11 - Time evolution of membrane and contact resistance, $R_{m,c}$ (HFR), during cold start [29].

The key cold start findings from existing literature are summarized in Table 1.1 below.

Table 1.1 - Comparison of existing cold start literature

Parameter / Diagnostic	Key Results	Comments
Membrane water content, λ	Dry membrane (low λ) beneficial	Increases membrane water storage capacity; results in longer cold start duration until freeze-out [10,15-19]
Shut down purge technique	Dry shutdown purge beneficial; gives low λ	Produces more water during cold start [10,17,20]
		Increases chances of self-start [20,21]
		Reduces freeze/thaw damage [12-14,23,24]
Startup current density, i	Low i beneficial	Produces more water during cold start [10,17,19,25]
		Allows more uniform water and ice distribution in cathode CL [10]
Dry air flow rate	High flow rate beneficial	Removes more product water before freeze-out [15,16,22]
Phase of product water on cathode CL	Liquid water can exist at -10°C [26,27]	Contradictory with [20,28]
	Liquid water cannot exist <-1.5°C [20,28]	Contradictory with [26,27]
HFR	HFR decreases during cold start	Due to PEM dehydration [10,15,29]
	HFR increases at the end of cold start [29]	Due to increased contact resistance; not addressed in [10,15]

1.4 Objectives

This summary in Table 1.1 reveals that a gap in fuel cell literature exists regarding the behavior of cell resistance during cold start. This discrepancy gives a motivation to perform experimental cold starts from -10°C to elucidate the behavior of cell resistance before, during, and after cold start. The objective of this study is to develop cell resistance as a diagnostic tool for cold start performance as well as an indicator for the level of water present in the membrane and CL. Furthermore, the effect

of startup current density on cold start performance, cell resistance, and CL ice formation is investigated. Additionally, it is desired to develop experimental techniques to allow for rapid and repeatable cold starts since existing approaches require lengthy reconditioning and purge procedures after freeze-out occurs.

Chapter 2 Method of Approach

2.1 Experimental Setup

A single 5 cm^2 parallel-channel cell was used in this study. The flow fields consist of 13 straight, parallel channels each measuring 23 mm long by 1 mm wide and 0.4 mm and 0.6 mm deep on the anode and cathode, respectively. The lands measure 0.75 mm wide, giving a land to channel ratio of 0.75. The flow field plates are 1.3 cm thick gold-plated stainless steel which also serve as current collectors. Outside of the flow field plates are hollow aluminum end plates to allow coolant fluid to pass through for high-temperature isothermal management.

The MEA used were reinforced Gore™ Primea® 57 series with 0.4 mg/cm^2 Pt loading on each electrode and a dry membrane thickness of 18 μm. Sigracet® SGL 10BB, carbon paper with microporous layer and 5% PTFE additive, areal weight of 125 g/m^2, measuring 420 μm ± 70 μm thick, was used as DM for both the anode and cathode. The heat capacity of the fuel cell itself is much greater than that of the MEA; therefore the heat generated by the electrochemical reaction has a negligible impact on the channel and land boundary temperature during operation. This results in an experimental isothermal boundary condition, although the local membrane and CL temperature can rise during current draw.

A schematic of the experimental configuration is shown in Figure 2.1. An Arbin fuel cell test station controlled the electronic load as well as gas flow rates and dew

points. When above freezing, cell temperature was controlled by a Brookfield thermal bath (model EX-200) by passing coolant water at a high flow rate of 2.3 L/min through the coolant channels in the end plates of the cell to assure isothermal operation. A Tenney environmental chamber (model/serial TJR/33631) was used to cool down and sustain cell temperature at -10°C. During cold start, the gas inlet lines to the cell were coiled inside the chamber to allow the reactants to sufficiently cool to the temperature of the chamber. The Arbin humidifiers were bypassed during cold start to ensure dry reactant gas flow. Throughout experiments HFR measurements were taken to quantify cell resistance using a 5 mA AC current at 3 kHz frequency.

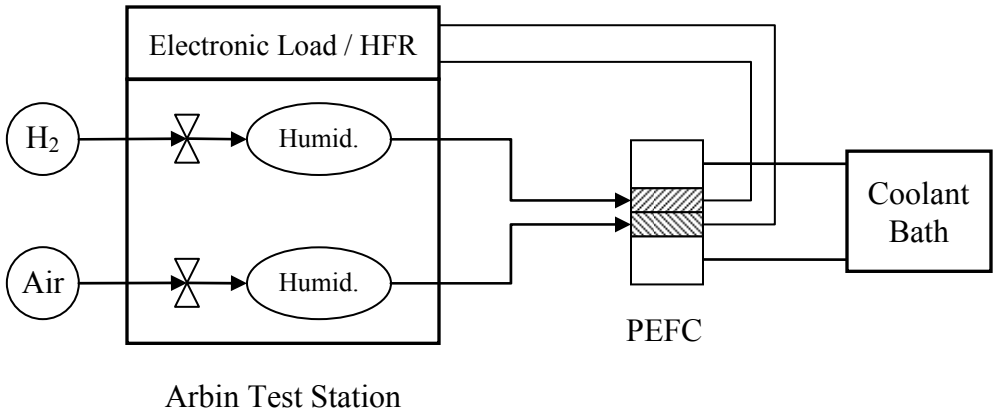

(a)

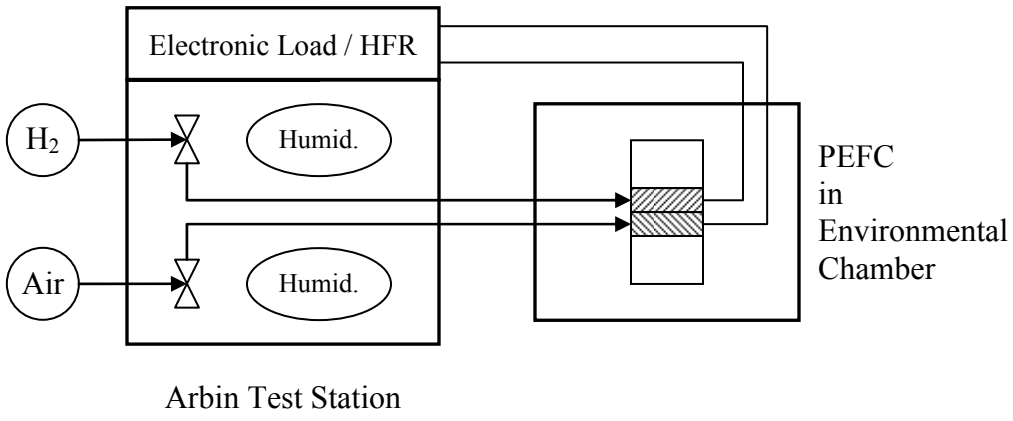

(b)

Figure 2.1 - Schematic of test configuration for: (a) initialization, performance testing, and equilibrium purge, (b) cool down and cold start testing.

2.2 Experimental Procedure

The experimental procedure consisted of four steps: initialization, an extended purge to achieve uniform water distribution within the cell (equilibrium purge), cool down, and consecutive cold starts. After normal preconditioning at 65°C and a baseline performance measurement, the cell was initialized at this same temperature by operation at 600 mV for 30 min under fully saturated conditions, i.e. 100% RH. Hydrogen was supplied to the anode at 0.45 L/min while air was supplied to the cathode at 1.07 L/min (each flow rate is equivalent to a stoichiometry of 12 at 1.0 A/cm^2). These high flow rates were required to prevent flooding due to the parallel channel design.

The cell was then allowed to cool by natural convection to 37°C for equilibrium purging. The main goal of the equilibrium purge was to achieve a known low membrane water content prior to cool down. A cell temperature of 37°C was chosen to allow the MEA to achieve a dry state during purge while the humidifiers were held at room temperature. Keeping the humidifiers at room temperature ensured that an insignificant amount of water condensed inside the cell as it cooled to -10°C. During purging, 40% RH N_2 at 1.07 L/min was fed into the anode and cathode for an extended period of time, which gave a known water activity, a, upon completion. The membrane boundary water activity could then be related to membrane water content, λ, by the Springer relationship [5] given by Eq. 1.2. The purge was cycled on and off to determine when equilibrium in all cell components was obtained, since residual water in the DM or CL can rehydrate the membrane. During the off cycle of the purge process, the inlets and outlets of the cell were closed, which allowed the water distribution throughout the MEA and DM to equilibrate to remove any concentration differences that may occur through the MEA|DM

structure during purging. The specific details of the purge cycle used to achieve a uniform water distribution of λ = 3.1 for this cell are given in Table 2.1 and explained further in Section 3.1.

Table 2.1 - Experimental procedure for equilibrium purge cycle (RH = 40%, λ = 3.1)

Step	Stage	Duration	N_2 flow rate (L/min)		Gas dew point	Cell temperature
		(min)	Anode	Cathode	(°C)	(°C)
I	Purge	180	1.07	1.07	21	37
II	Relaxation	60	0	0	-	37
III	Purge	30	1.07	1.07	21	37
IV	Relaxation	30	0	0	-	37
V	Purge	30	1.07	1.07	21	37
VI	Relaxation	30	0	0	-	Natural cooling

After the equilibrium purge, the cell was placed in the environmental chamber and cooled to -10°C. The cell inlets and outlets remained closed in order for λ to stay constant during cool down: the volume of the flow field channels is 0.3 cm^3 which can condense 4 μg of water during cool down from the dew point of 21°C to -10°C. This amount of water, if fully absorbed by the membrane, gives an increase in λ of only 0.01, which can be neglected. Therefore, λ is assumed to remain constant at 3.1 during the cool down procedure. The cool down process took approximately 2.5 hrs, which included a 1 hr soak at -10°C to allow a uniform temperature distribution throughout the cell. All cold starts performed in this study occur from -10°C. Prior to cold start, the test

station was also purged with dry gas directly from the gas cylinders to remove any residual water that may have accumulated in the pipelines during initialization or purging.

After the cell was sufficiently temperature soaked, dry reactant gases at -10°C were fed into the cell at 0.15 L/min and 0.30 L/min (equivalent stoichiometries of 2.7 and 3.4 at 1.0 A/cm^2) at the anode and cathode, respectively, to allow for OCV stabilization. Cell resistance was recorded and once reaching a specific value (0.30 Ω cm^2 unless otherwise specified) the flow rates were changed to 0.05 L/min and 0.11 L/min (equivalent stoichiometries of 12 and 12 at 0.1 A/cm^2) at the anode and cathode, respectively. A cold start was then initiated by drawing a constant current from the cell while cell voltage and resistance were recorded. When cell voltage dropped below a set value (50 mV) due to freeze-out, the electronic load was automatically shut off. In this study, cold start performance was measured by the amount of water produced during startup, given by Eq. 1.4.

It was found that if dry gas continued to flow through the cell after freeze-out (termed cold purge), OCV re-stabilized due to ice removal by sublimation, and consecutive cold starts could be rapidly performed without the necessity of heating, initializing, and purging the cell again. Cold purging was performed by setting the flow rates back to 0.15 L/min and 0.30 L/min at the anode and cathode, respectively. Once the cell resistance again reached a specific value, the flow rates were changed back to 0.05 L/min and 0.1 L/min on the anode and cathode, respectively, and another cold start could be performed. This cold purge / cold start / cold purge process could then be repeated. The performance of such successive cold starts was quite repeatable and representative of

the same behavior seen after a full equilibrium purge. The process is described in more detail in the following sections.

Chapter 3 Results and Discussion

3.1 Cell resistance during equilibrium purge and cool down

Cell resistance observed during the equilibrium purge is shown in Figure 3.1. As can be seen, resistance increases and plateaus at 0.22 Ω cm^2 during purge periods. During the relaxation periods, resistance decreases due to water redistribution throughout the MEA. The final relaxation period shows a slight increase in resistance because the cell is naturally cooling to room temperature, which decreases membrane conductivity. During purge steps, resistance consistently plateaus around 0.22 Ω cm^2, indicating that at the completion of any purge period the membrane water content is consistently $\lambda = 3.1$.

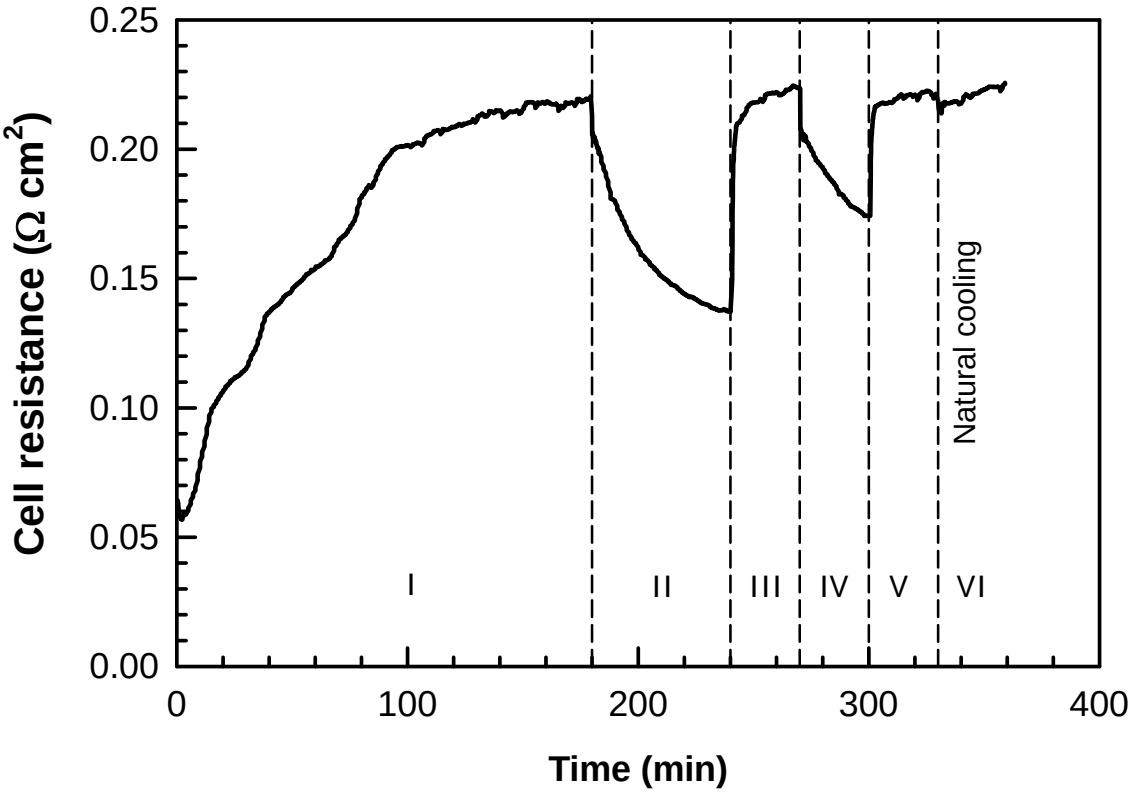

Figure 3.1 - Cell resistance during 40% RH N_2 purge (λ = 3.1). The cell was consecutively purged and relaxed, as labeled.

Membrane proton conductivity was measured while the cell cooled from room temperature to -10°C, as shown in Figure 3.2. Shown in the Arrhenius form, the σ - T relationship for λ = 3.1 shows no noticeable change in slope as the cell cools below freezing, indicating no phase change of water inside the membrane or any appreciable increase in contact resistance. The case of λ = 14 was obtained with a fully humidified membrane, and is used as a comparison to the data obtained by Tajiri *et al.* [10]. As can be seen, σ - T curve determined in the present study shows a convex shape. This behavior was also observed by Tajiri *et al.* [10] especially so at temperatures below -

10°C. As described previously, this is believed to be a result of a phase change of water in the membrane and/or an increase in contact resistance due to ice lens formations between the MEA sublayers. In general, higher conductivities were observed in comparison with data obtained by Tajiri *et al.* [10]. This was also reported by Beuscher *et al.*, [9] where it was shown that thinner membranes with lower equivalent weights demonstrate higher conductivity values.

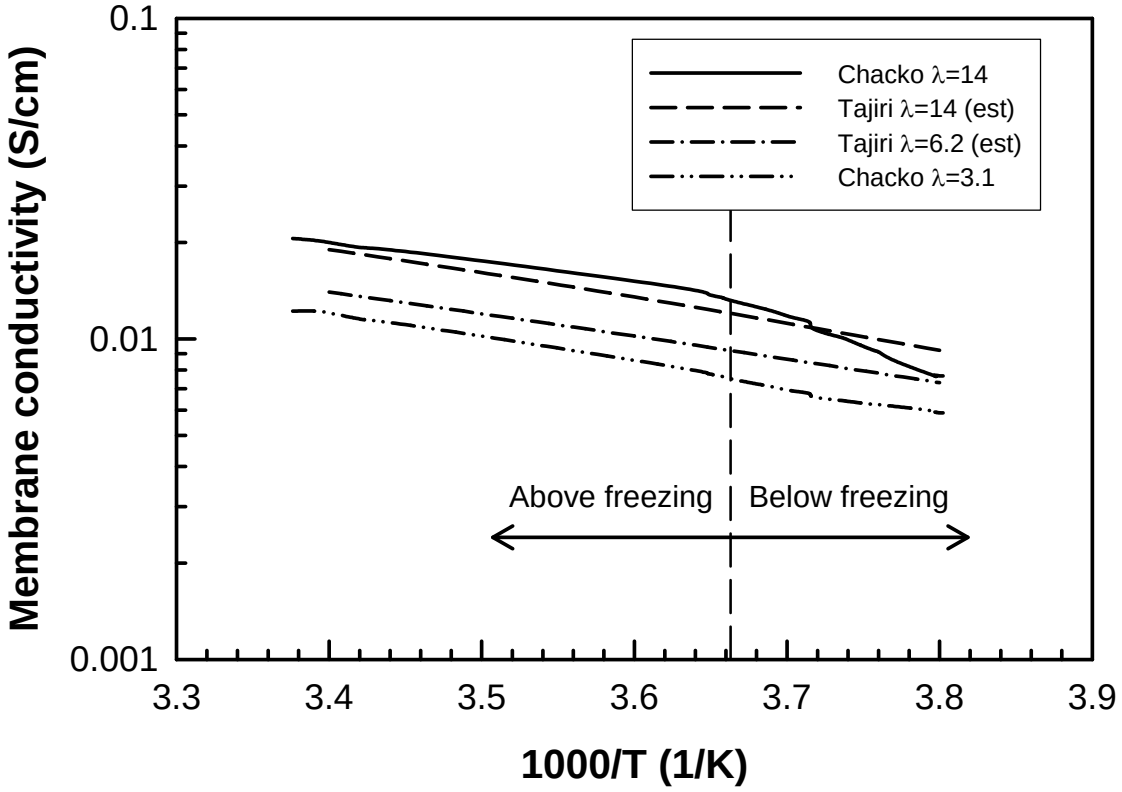

Figure 3.2 - Membrane proton conductivity as a function of temperature and λ during cool down from room temperature to -10°C with comparable data from Tajiri *et al.* [10].

3.2 Consecutive cold starts

The behavior of cell resistance during a set of consecutive cold starts can be seen in Figure 3.3. Note that gas flows through the cell during the entire test, but current is only being drawn from the cell during a startup. During a startup cell resistance decreases due to membrane hydration then increases due to ice formation in the cathode CL. Between cold starts cell resistance decreases due to residual ice removal from the cathode CL then increases due to membrane dehydration. These four processes are described in detail in the following sections.

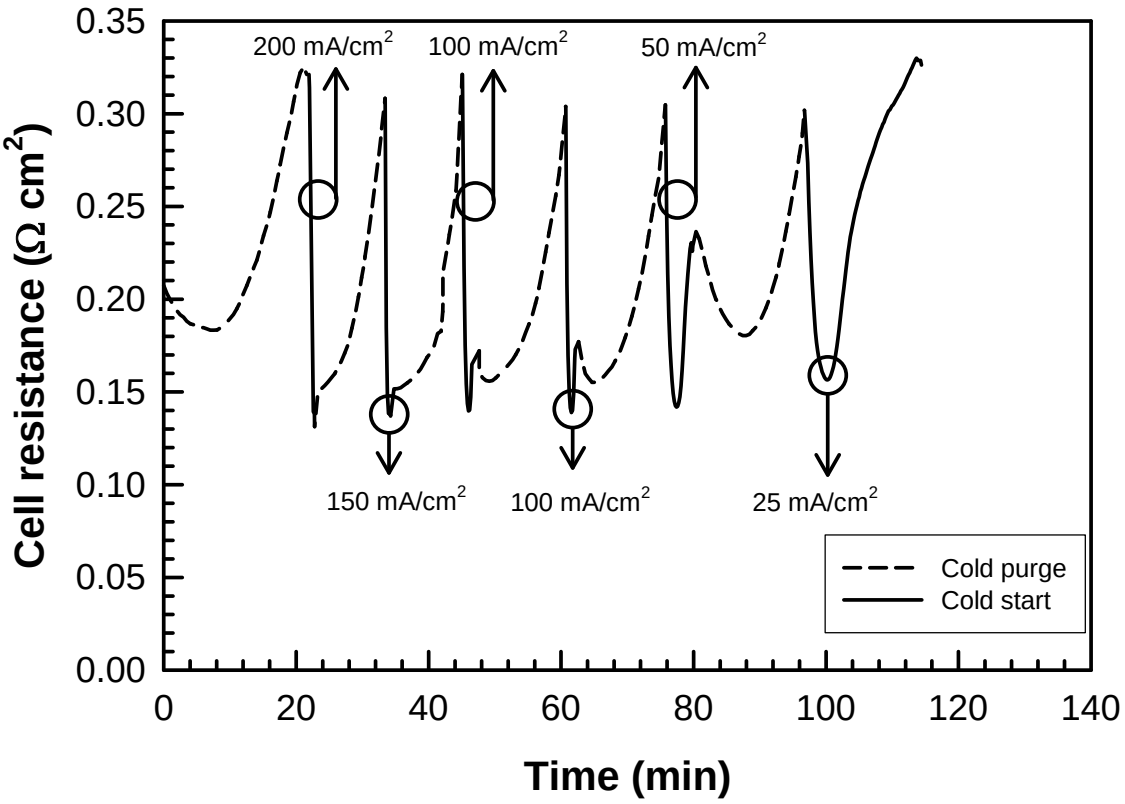

Figure 3.3 - Cell resistance behavior during a set of consecutive cold starts from various startup current densities.

As shown in Figure 3.3, the cold starts were initiated once the cell reached a specific resistance value, here 0.30 Ω cm^2, at startup current densities ranging from 200 mA/cm^2 to 25 mA/cm^2. The case of i = 100 mA/cm^2 was performed twice to ensure the repeatability of tests. Performance proved to be identical: 0.80 mg/cm^2 of water was produced during each startup and the final resistance recorded at freeze-out was 0.17 Ω cm^2 for each case.

A separate study was conducted in order to determine if any difference existed between a startup performed after the long, elevated temperature equilibrium purge compared to one performed in the middle of a set of rapid consecutive cold starts. A cold start performed after the equilibrium purge and a cold start performed in the middle of a consecutive set showed less than a 5% difference in voltage and startup time. Furthermore, when the same type of startups shown in Figure 3.3 were performed in random order, a negligible difference in voltage and startup time was found.

This repeatability indicates that consecutive cold starts can be used as a rapid, efficient, and repeatable cold start procedure. To compare, the conventional published method requires a four step process including high temperature initialization, equilibrium purging, cool down, and cold soak for each cold start performed, which requires approximately seven hours of preparation for only one cold start. Then after the cold start is initiated and a freeze-out occurs, this seven hour procedure must be repeated. The method of rapid consecutive cold starts uses the same four aforementioned steps, but the use of the 15 minute cold purge after freeze-out allows for an indefinite amount of cold starts to be performed without having to reheat the cell. Thus, this approach significantly

reduces experimental time in comparison to conventional methods and may be used as a rapid and repeatable method to assess cold performance, degradation, and other metrics of interest.

3.2.1 During cold start

The startups at i = 100 mA/cm^2 and i = 50 mA/cm^2 from Figure 3.3 are enlarged in Figure 3.4a and Figure 3.4b, respectively. The cell voltage first sharply drops from OCV due to the load applied to the cell. Voltage then slightly increases while resistance decreases, due to membrane hydration by the product water. Hydrating the membrane increases proton conductivity which improves performance (voltage) and decreases resistance, and is consistent with previous publications [10,15,29].

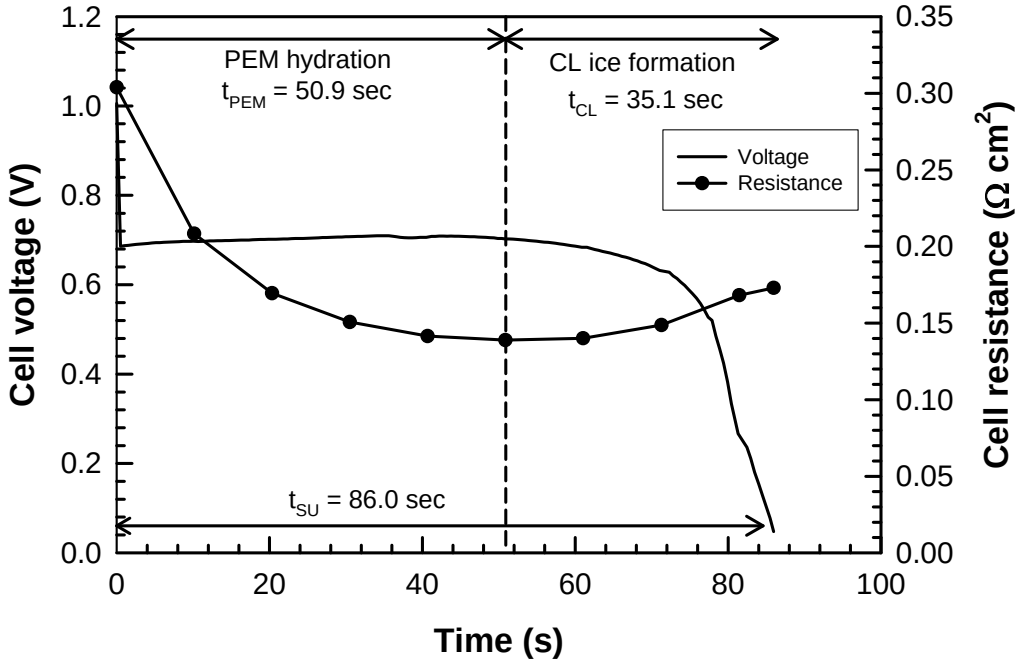

(a)

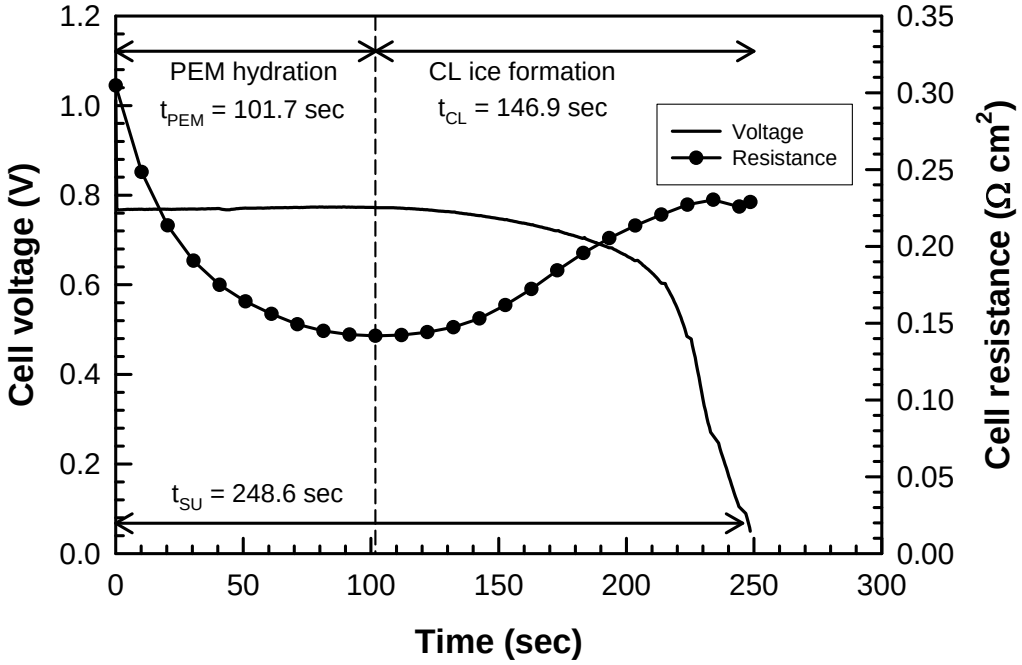

(b)

Figure 3.4 - Cell voltage and resistance behavior during cold start for: (a) *i* = 100 mA/cm^2 (b) *i* = 50 mA/cm^2.

After a certain membrane water uptake capacity is reached, voltage begins to decrease while cell resistance increases. This behavior is attributed to ice formation in and around the cathode CL. As ice is formed, it begins to cover reaction sites and reduce the electrochemical surface area and as a result cell voltage decreases. Eventually, the ice completely blocks the CL reaction sites and the electrochemical reaction ceases. Ice should not affect the HFR by merely filling open pores in the CL or DM. This measured resistance increase is therefore indicative of some interfacial ice lens production or contact loss due to ice expansion.

To verify that this resistance increase is indeed a result of ice external to the membrane and not a result of a phase change of water inside the membrane, a cold start was performed but stopped once resistance reached its minimum during startup, which occurs well before freeze-out. The load was removed from the cell and the inlets and outlets were closed, allowing any product water to freeze in the membrane. Resistance was observed to stabilize near the minimum value, indicating a phase change of the water in the membrane was not responsible for the HFR increase observed during freeze-out.

A simple water balance was performed during cold start, following the modes of transport illustrated in Figure 3.5. Initially during startup, the product water is absorbed by the membrane, shown in Figure 3.5a. Once the membrane water uptake capacity is reached, the water begins to fill in and around the cathode CL and freeze, as shown in Figure 3.5b. It should be noted that, in reality, these two processes might occur in parallel. For analysis purposes, it is assumed that no water freezes in the DM due to low vapor saturation pressure associated with cold start [18]. Water can be removed from the cell by the anode or cathode gas streams. The effects of electro-osmotic drag (EOD) and

back diffusion (BD) are not directly calculated but are incorporated within the calculations of water transport into the membrane or into the cathode CL. For instance, the amount of water that the membrane absorbs, calculated from experimental findings, is affected by the processes of EOD and BD. Therefore, although EOD and BD are not directly calculated, they are incorporated into the water balance.

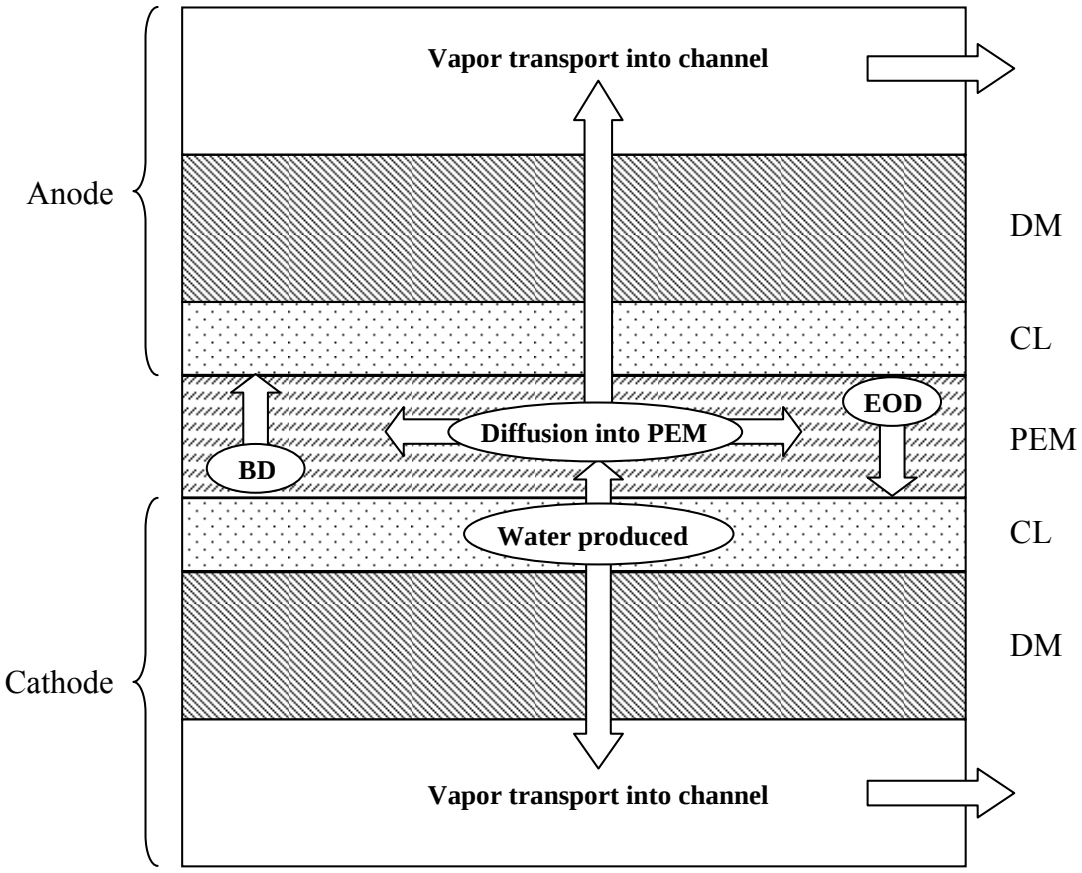

(a)

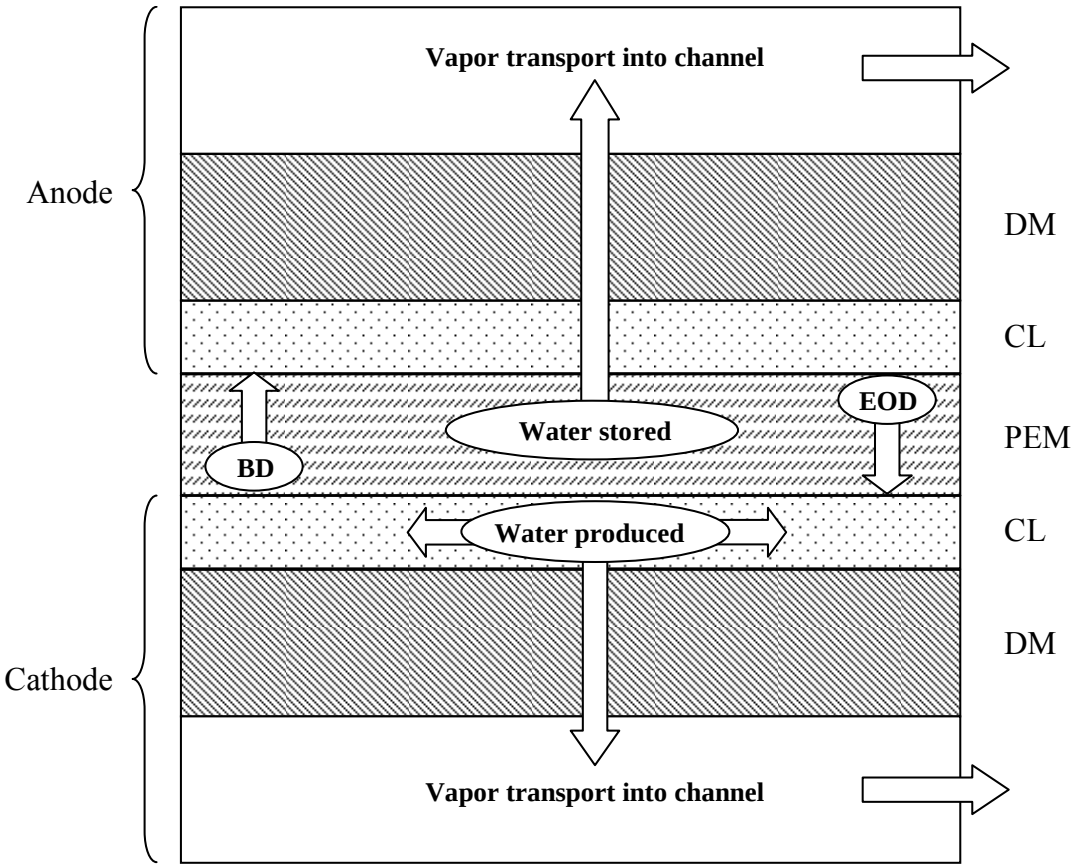

(b)

Figure 3.5 - Water transport during cold start: (a) Membrane rehydration, (b) Catalyst layer ice filling (not to scale). EOD = Electro-osmotic drag, BD = Back diffusion.

If the dry reactant gas exits the cell fully saturated, the maximum amount of water removed from the cell is given as [1]:

$$m_{rem} = \left(\dot{n}_a + \dot{n}_c\right)\frac{P_{sat}(T)}{P_{cell} - P_{sat}(T)} M_{H_2O}\,\Delta t \approx \left(\dot{n}_a + \dot{n}_c\right)\frac{P_{sat}(T)}{P_{cell}} M_{H_2O}\,\Delta t \tag{3.1}$$

where $\dot{n}$ is the molar flow rate of the anode or cathode gas stream, $P_{sat}(T)$ is the saturation pressure of water vapor over either ice or liquid water, P_{cell} is the pressure of the cell, M_{H_2O} is the molecular weight of water, and Δt is the duration of gas flow.

Eq. 3.1 assumes that the gas stream leaving the cell is fully saturated, which may not be the case, depending on the particular cell and operating conditions. In order to approximate the actual saturation level, desiccant bottles were attached to the anode and cathode exits of the cell in order to collect the water that is removed by the dry reactant gas streams. This was performed over the course of the set of six consecutive cold starts shown in Figure 3.3. It was found that only 17% and 45% of the amount of water calculated by Eq. 3.1 was actually collected at the anode and cathode, respectively. The low exit saturation level of the anode is expected due to the relatively dry state of the anode during cold start. Based on these calibration tests, the amount of water that actually is removed from the cell during cold start testing is given as:

$$m_{rem} = \left(0.17\dot{n}_a + 0.45\dot{n}_c\right)\frac{P_{sat}(T)}{P_{cell}} M_{H_2O}\,\Delta t \tag{3.2}$$

It should be noted that Eq. 3.2 is a water removal calculation assuming constant 17% and 45% saturation levels throughout the entire duration of the set of cold starts. These saturation percentages are dependent on flow rate, water diffusivities through MEA components, and water saturation levels of these components. However, calculations are performed assuming constant saturation percentages of the exit gases throughout the set of cold starts.

The water produced during cold start, m_{pro}, is given by Eq. 1.4 where $t = t_{SU}$ from Figure 3.4. The amount of water removed from the cell, m_{rem}, can be determined from Eq. 3.2, where $\Delta t = t_{SU}$ from Figure 3.4. Therefore, the total water stored in the cell, m_{sto}, is given as:

$$m_{sto} = m_{pro} - m_{rem} \tag{3.3}$$

The water stored in the cell is utilized for either membrane hydration or cathode CL ice formation. During cold start, the membrane stores an amount of water, $m_{PEM,act}$, given by:

$$m_{PEM,act} = m_{sto} \cdot \frac{t_{PEM}}{t_{SU}} \tag{3.4}$$

where t_{PEM} and t_{SU} are determined from Figure 3.4. The maximum amount of water that the membrane can store, $m_{PEM,\max}$, given as:

$$m_{PEM,\max} = M_{H_2O} \cdot \delta_{PEM} \frac{\rho_{dry}\left(\lambda_{sat} - \lambda_i\right)}{EW} A \tag{3.5}$$

Typical membrane properties are assumed: δ_{PEM} = 18 μm, ρ_{dry} = 2000 kg/m^3, EW = 0.95 kg/mol, and λ_{sat} = 14. Since the membrane is dried to some degree prior to startup, the exact value of λ_i, the initial membrane water content prior to startup, is difficult to determine (see Section 3.2.2) but it is assumed the membrane is dried to $\lambda_i < 3.1$ prior to startup. For water storage calculation purposes only, we consider the membrane to be *completely* dry at startup, i.e. λ_i = 0.043. This assumption accounts for the absolute

maximum amount of water the membrane can uptake (although it is not realistic to fully dry the membrane).

The amount of water that is utilized for cathode CL ice formation, $m_{CL,act}$, is given as:

$$m_{CL,act} = m_{sto} \cdot \frac{t_{CL}}{t_{SU}} \tag{3.6}$$

where t_{CL} and t_{SU} are determined from Figure 3.4. The maximum amount of ice that the cathode CL can store, $m_{CL,\max}$, is given as:

$$m_{CL,\max} = \delta_{CL}\left(\varepsilon_{CL}\rho_{ice} + \lambda_{sat}\varepsilon_{CL,e}\frac{\rho_{dry}}{EW}M_{H_2O}\right)A \tag{3.7}$$

The left term in parentheses of Eq. 3.7 represents the amount of water that can be stored in the pores of the cathode CL while the right term represents the amount of water that can be stored in the electrolyte phase of the cathode CL. Typical CL properties are assumed: δ_{CL} = 10 μm, ε_{CL} = 0.6, and $\varepsilon_{CL,e}$ = 0.2. To account for the maximum cathode CL ice storage capacity, it is assumed the CL is completely free of ice prior to startup and becomes fully saturated at freeze-out, i.e. λ_{sat} = 14.

The calculated quantities of the water balance for the cold starts shown in Figure 3.3 are given in Table 3.1. As can be seen, the actual amount of water stored in the membrane is relatively constant for all cases, indicating that using a lower startup current density does not allow for more utilization of the membrane storage capacity. In other words, there is a maximum amount of water that the membrane can uptake during cold start before the CL begins to fill with ice, regardless of startup current density, at least for

the cell tested. Even if it is assumed that water diffusion out of the membrane is extremely low and the membrane dehydration region prior to startup keeps the membrane at λ_i = 3.1 (and not completely dry as assumed for maximum storage calculations), the membrane storage utilization only increases to 62% for the i = 100 mA/cm^2 case, again indicating the membrane is not fully saturated at freeze-out.

Table 3.1 - Water balance during cold starts

		Startup current density, i (mA/cm^2)					
		25	50	100	100	150	200
	Unit	Value					
Overall							
t_{SU}	sec	1060.8	248.6	86	85.6	49.2	34.3
m_{pro}	mg/cm^2	2.47	1.16	0.80	0.80	0.69	0.64
m_{rem}	mg/cm^2	0.38	0.09	0.03	0.03	0.02	0.01
m_{sto}	mg/cm^2	2.09	1.07	0.77	0.77	0.67	0.63
PEM hydration							
t_{PEM}	sec	183.1	101.7	50.9	51.9	30.5	27.3
$m_{PEM,act}$	mg/cm^2	0.36	0.44	0.46	0.47	0.42	0.50
$m_{PEM,max}$	mg/cm^2	0.95	0.95	0.95	0.95	0.95	0.95
$(act/calc)_{PEM}$	mg/cm^2	38	46	48	49	44	52
CL ice formation							
t_{CL}	sec	877.7	146.9	35.1	33.7	18.7	7.0
$m_{CL,act}$	mg/cm^2	1.73	0.63	0.31	0.30	0.25	0.13
$m_{CL,max}$	mg/cm^2	0.65	0.65	0.65	0.65	0.65	0.65
$(act/calc)_{CL}$	mg/cm^2	268	98	49	47	39	20

In order to analyze this membrane water storage phenomenon, the time constant for diffusion through the membrane can be found using:

$$\tau_{diff} = \frac{\delta_{PEM}^{\ 2}}{D} \tag{3.8}$$

Taking the minimum diffusion constant of water into the membrane over various λ ($D = 6 \times 10^{-12}$ m^2/sec) [30], this time constant is calculated to be 54 sec. Based on the time associated with membrane hydration for i = 25 mA/cm^2 (t_{PEM} = 183 sec), the product water should have ample time to fully diffuse into the membrane. However, much less than the maximum membrane storage capacity is utilized. It is concluded that there is some maximum membrane water content increase, $(\Delta\lambda)_{\max}$, that can be achieved during cold start before ice begins to form. The average membrane water storage of 0.44 mg/cm^2 gives a $(\Delta\lambda)_{\max}$ = 6.4 according to Eq. 3.5. Therefore, in order to optimize cold start performance by keeping the membrane as hydrated and conductive as possible but also allowing it to store 0.44 mg/cm^2 of water, there is an optimal membrane water content prior to startup. This depends on the maximum water content of the membrane, $\lambda_{\max}$, before ice begins to form. For instance, if $\lambda_{\max}$ = 14 in a frozen state, the optimal membrane water content prior to startup would be λ_i = 7.6. That is, as λ increases from 7.6 to 14 during cold start, the membrane can store 0.44 mg/cm^2 of product water while also staying as conductive as possible. An initial condition of $\lambda_i <$ 7.6 would not serve any purpose, as the additional capacity could not be utilized before ice begins to form.

On the other hand, the amount of water that freezes in the cathode CL increases as startup current density decreases. This implies that a lower current density allows for water to distribute itself more within the CL prior to freeze-out which is consistent with existing literature [10]. However, for i = 25 mA/cm^2 the actual ice produced is over two times greater than the cathode CL storage capacity. This indicates that some of the water stored during cold start emerges out of the cathode CL and is stored in the DM, also reported by Mao *et al.* [19]. The fact that this water has the ability to be transported out of the CL may be indicative of the presence of super-cooled liquid water, as observed by Ishikawa *et al.* [26,27] at -10°C. This water then freezes inside the DM or gas channels. The effect of ice production on cell resistance is examined later in this study.

3.2.2 Between cold starts

Resistance behavior between cold starts (during the cold purge) is a direct consequence of the dry gas removing residual product water/ice from the cell. Figure 3.6 shows cell resistance behavior between the cold start of i = 50 mA/cm^2 and i = 25 mA/cm^2 (note no current is being drawn from the cell). Resistance is seen to initially decrease due to residual ice removal from the CL. Once this ice is removed from the CL, resistance then increases due to membrane dehydration. Again, these processes may occur in parallel as well.

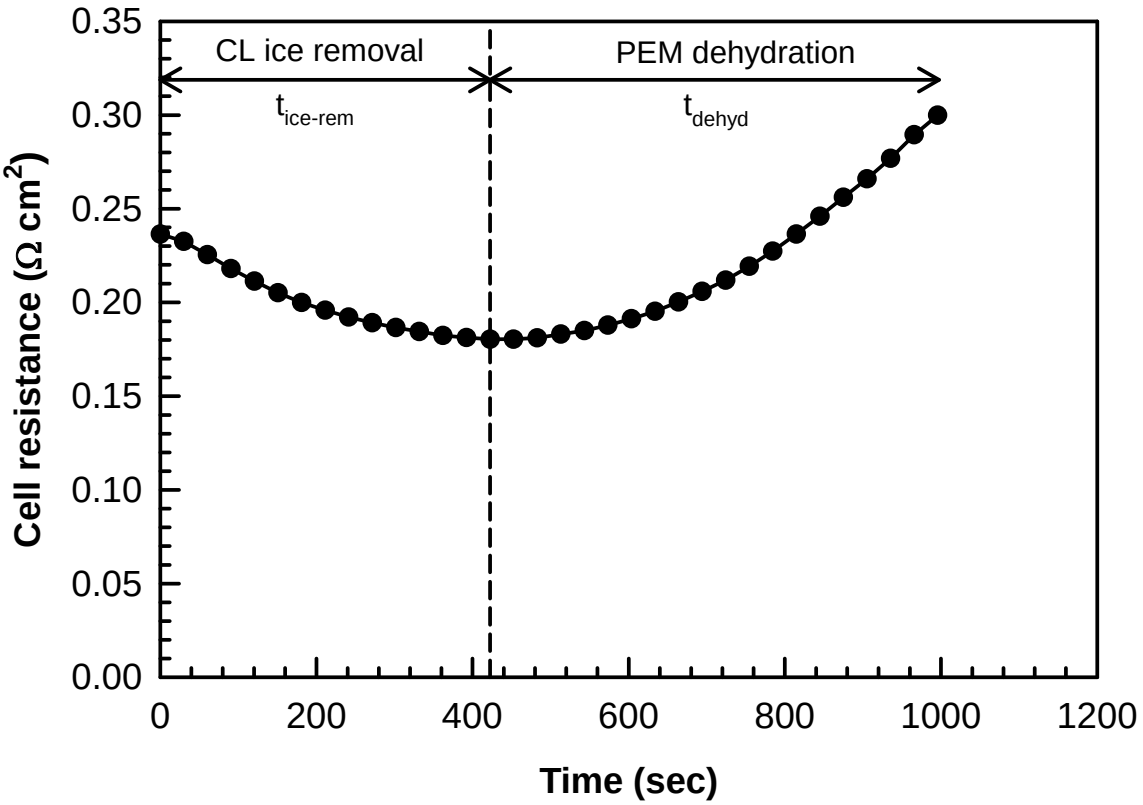

Figure 3.6 - Cell resistance behavior between cold start, after i = 50 mA/cm^2 and prior to i = 25 mA/cm^2 startup. Gas flows through cell while OCV stabilizes.

A simple water balance was performed on Figure 3.6. It should be noted that while the cathode gas stream first removes ice from the cathode CL and then begins to dehydrate the membrane, the anode gas stream is believed to only dehydrate the membrane since there is very little water to remove from the anode CL. The amount of ice removed from the cathode CL can be found using Eq. 3.2 and accounting for only the cathode gas stream, where $\Delta t = t_{ice-rem} = 422\,\text{sec}$. The amount of water removed from the membrane can be found using Eq. 3.2 as well, and accounting for each gas stream

separately; $\Delta t = t_{dehyd,a} = 996\,\text{sec}$ and $\Delta t = t_{dehyd,c} = 574\,\text{sec}$ for the anode and cathode, respectively. The amount of ice or water that was stored in the CL or membrane is given in Table 3.1 as $m_{CL,act}$ and $m_{PEM,act}$, respectively. Based on this water balance, it is found that the removal calculation underestimates the CL ice storage by 42% and overestimates the membrane water storage by 66%. The reason for this discrepancy is believed to be a result of the parallel processes of membrane hydration & CL ice formation during startup as well as CL ice removal & membrane dehydration during cold purge. Furthermore, the specific saturation levels of the exit gases likely depend on the saturation level of water and the diffusivities of water out of each specific component.

Because of this discrepancy, an overall water balance analysis was performed during and after the cold starts shown in Figure 3.3 to validate Eq. 3.2. In order for the water balance to equate, the amount of water stored in the cell during the cold start, m_{sto}, must be equal to the water removed during cold purge after that particular cold start, m_{rem}. These values are shown in Table 3.2 and it is found that the total water removed overestimates the total water stored by only 0.06 mg/cm^2 during the entire set. This validates the conclusion that Eq. 3.2 correctly calculates the overall amount of water removed from the cell, but should not be used to specifically account for amount of ice removed from the CL versus the amount of water removed from the membrane.

Table 3.2 - Overall water balance during set of consecutive cold starts

		Startup current density, i (mA/cm^2)					
		200	150	100	100	50	Total
	Unit	Value					
m_{sto}	mg/cm^2	0.63	0.67	0.77	0.77	1.07	3.91
m_{rem}*	mg/cm^2	0.66	0.63	0.81	0.78	1.09	3.97
m_{sto} - m_{rem}	mg/cm^2	-0.03	0.04	-0.04	-0.01	-0.02	-0.06

* These values calculated after above listed cold start

3.3 Effect of startup current density

Figure 3.7 plots cold start performance, measured in amount of water produced, as a function of startup current density. It should be noted that the reactant gas flow rates, given in Chapter 2.2, remained consistent during these cold starts. Therefore the water stored in the cell is a more suitable performance measurement between the different startup current density cases. The final cell resistance, recorded at freeze-out, is also shown. Figure 3.7 shows that a lower startup current density does in fact give better cold start performance since a lower current density allows water to distribute more evenly in the CL before freeze-out [10]. This additional water in and around the CL leads to additional ice, which is indicated by a higher final resistance.

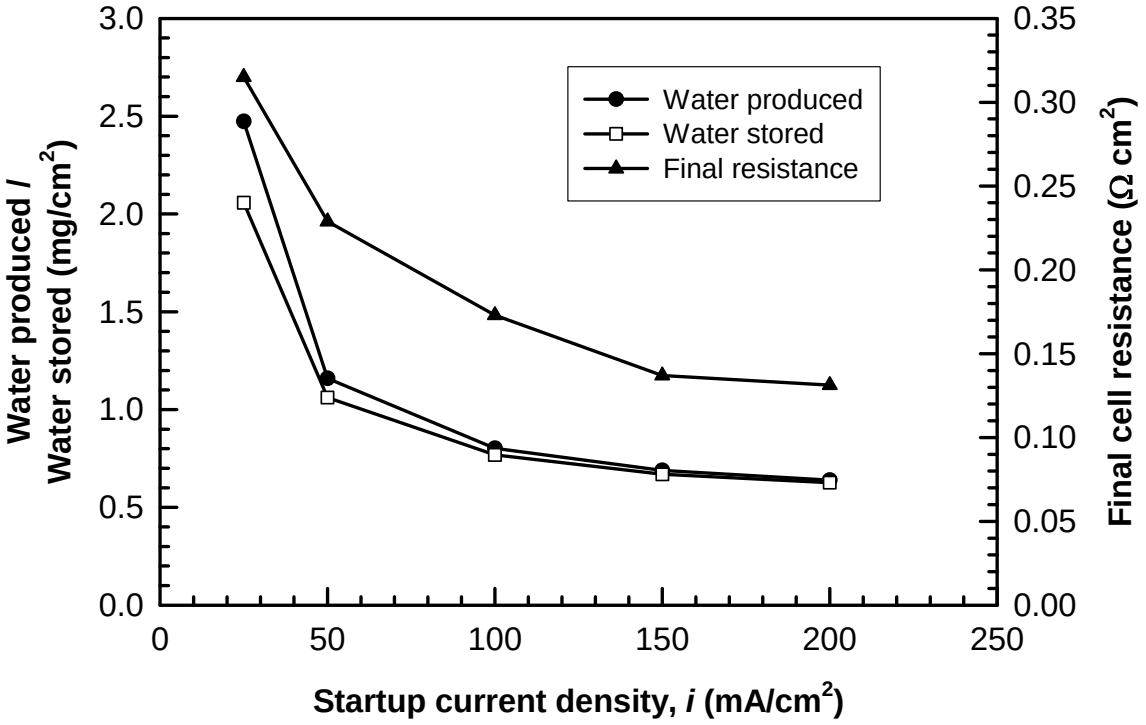

Figure 3.7 - Water produced, water stored, and final resistance during cold start as a function of startup current density.

Figure 3.8 demonstrates how the amount of ice stored during startup (reference $m_{CL,act}$ in Table 3.1) affects final cell resistance. The upper axis shows the ratio of ice stored during each cold start to the maximum storage capacity of the cathode CL. As more ice is stored during the CL ice formation stage of startup, ice fills in and around the cathode CL. Consequently, final cell resistance recorded at freeze-out increases. This trend demonstrates that cell resistance at freeze-out is an indicator of ice content in and around the CL.

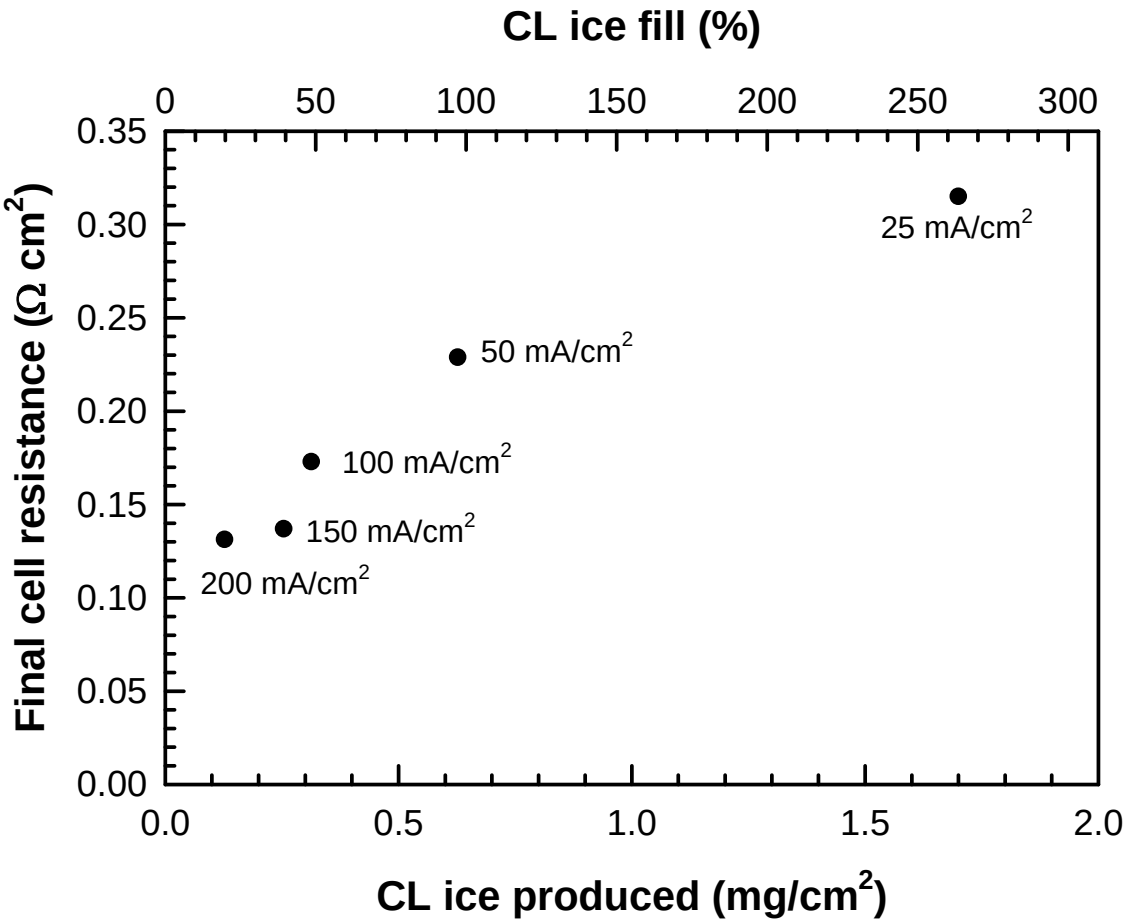

Figure 3.8 - Cell resistance recorded at freeze-out as a function of ice produced in the CL. Upper axis shows percentage of CL ice storage capacity utilized.

To further investigate the effect of water production on cell resistance values, the minimum resistance recorded during startup is plotted in Figure 3.9 as a function of the water produced during startup that is utilized for membrane hydration (reference $m_{PEM,act}$ in Table 3.1). In general, if more water hydrates the membrane, cell resistance is lower, which is expected, as the membrane hydrates, proton conductivity increases. However, this is not a particularly strong relationship. The maximum difference in resistance for this cell and these materials is only 18 mΩ cm^2. The upper axis in Figure 3.9 plots the

ratio of water utilized for membrane hydration to the maximum water storage capacity of the membrane, which is a weak function of startup current density. This further reinforces the point that the membrane can only absorb a certain amount of water during startup regardless of startup current density.

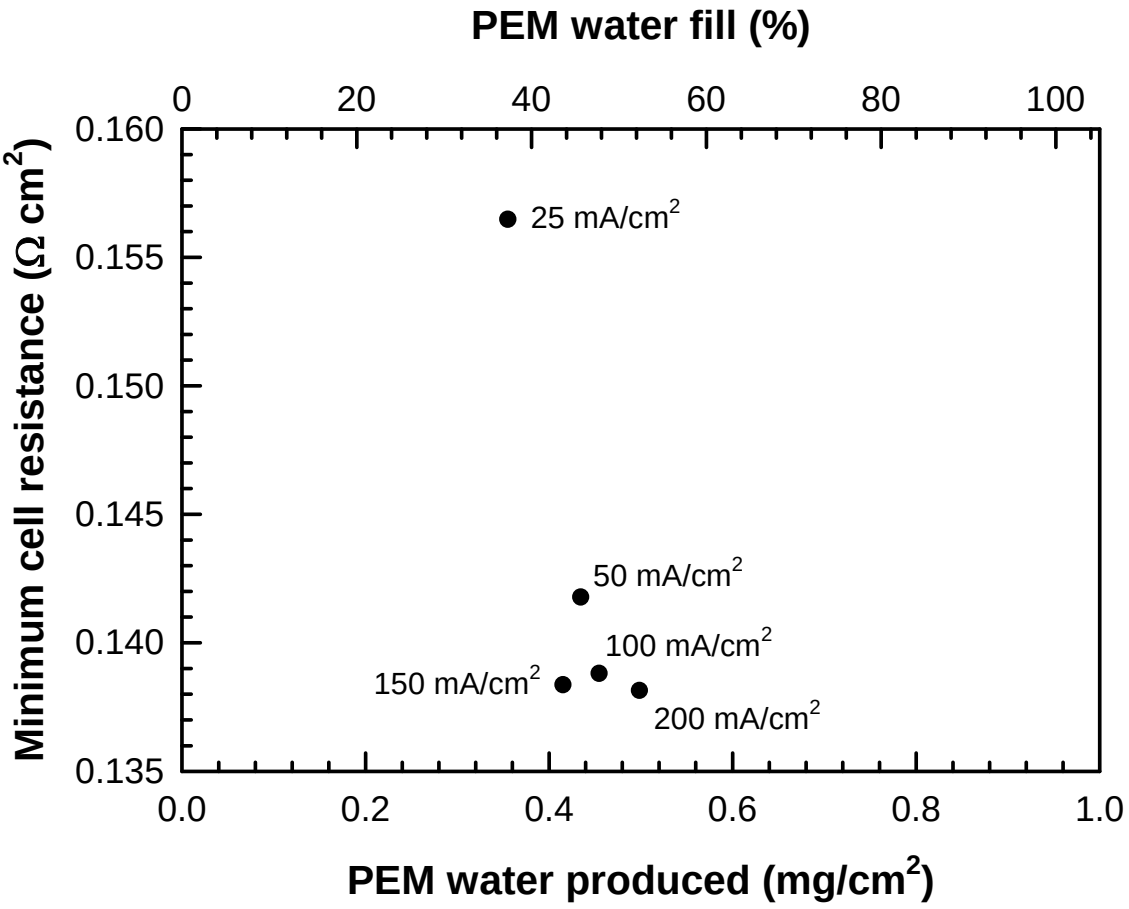

Figure 3.9 - Minimum resistance recorded during startup as a function of the water used for membrane hydration. Upper axis shows percentage of maximum membrane water storage capacity utilized.

Other useful performance measurements that can be extracted from these startups include the total energy produced (E) and total heat generated (Q) by the cell during cold start, given by:

$$E = \int_{t=0}^{t_{SU}} V_{cell}\, i\, A\, dt \tag{3.9}$$

$$Q = \int_{t=0}^{t_{SU}} \left(E_{th} - V_{cell}\right) i\, A\, dt \tag{3.10}$$

where V_{cell} is the actual cell voltage and E_{th} is the thermal potential (E_{th} = 1.48 V). Furthermore, the average energy generation rate ($\dot{E}_{avg}$) and average heat generation rate ($\dot{Q}_{avg}$) during cold start can be calculated by:

$$\dot{E}_{avg} = V_{cell,avg}\, i\, A \tag{3.11}$$

$$\dot{Q}_{avg} = \left(E_{th} - V_{cell,avg}\right) i\, A \tag{3.12}$$

These calculated quantities can be seen as a function of startup current density in Figure 3.10. Both total energy produced and total heat produced follow a power law relationship, indicating that a lower startup current density will be able to produce more usable energy as well as generate more heat to aid in self-start. This is attributed to lower startup current densities giving longer operation times before freeze-out; the total energy/heat produced is more dependent on startup time than current density in the range of parameters tested. However, when comparing the average production rates of energy and heat, it can be seen that these rates increase linearly as a function of startup current density. Therefore a compromise must be made between total energy/heat produced and their subsequent rates. This compromise can be used to provide an operational guideline for rapid stack startup. For instance, a certain fuel cell stack may have a minimum total heat required to self-start (indicated by the "hypothetical stack minimum" line in Figure

3.10). In order to generate sufficient heat for self-start and do so as rapidly as possible, a startup current density of approximately i = 90 mA/cm^2 would be optimal.

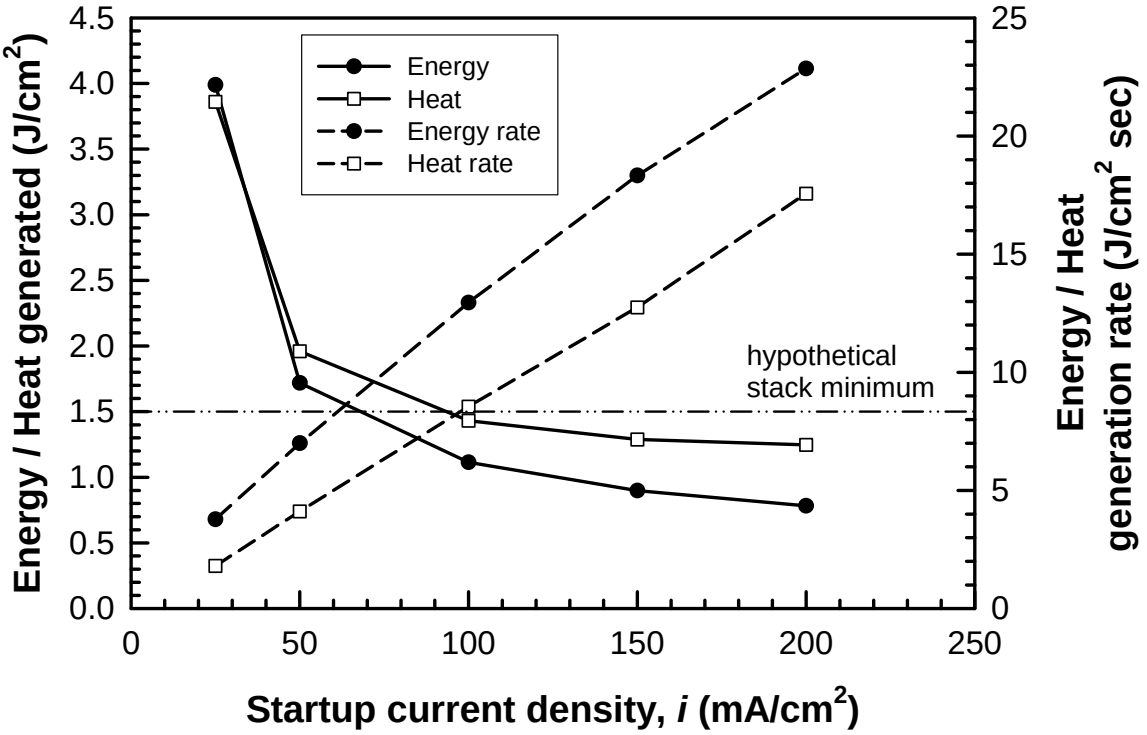

Figure 3.10 - Total energy produced, total heat produced, average energy production rate, and average heat production rate during cold start as a function of startup current density.

3.4 Predicting cold start performance with initial resistance

The results discussed so far conclude that the general hydration state of the MEA and the presence of residual ice can be described by measured HFR. Since cold start performance is highly dependent on MEA water content, the cell resistance recorded prior to startup may be used to predict performance. HFR is well suited for this

diagnostic due to its fast and non-intrusive nature. An additional set of experiments were performed to determine the range of resistance values that lead to optimal cold start performance. For these experiments, startup current density, flow rate, and cell temperature are identical for all cases; the only difference was initial cell resistance. Figure 3.11 shows cold start performance as a function of initial resistance for 50 different cold starts.

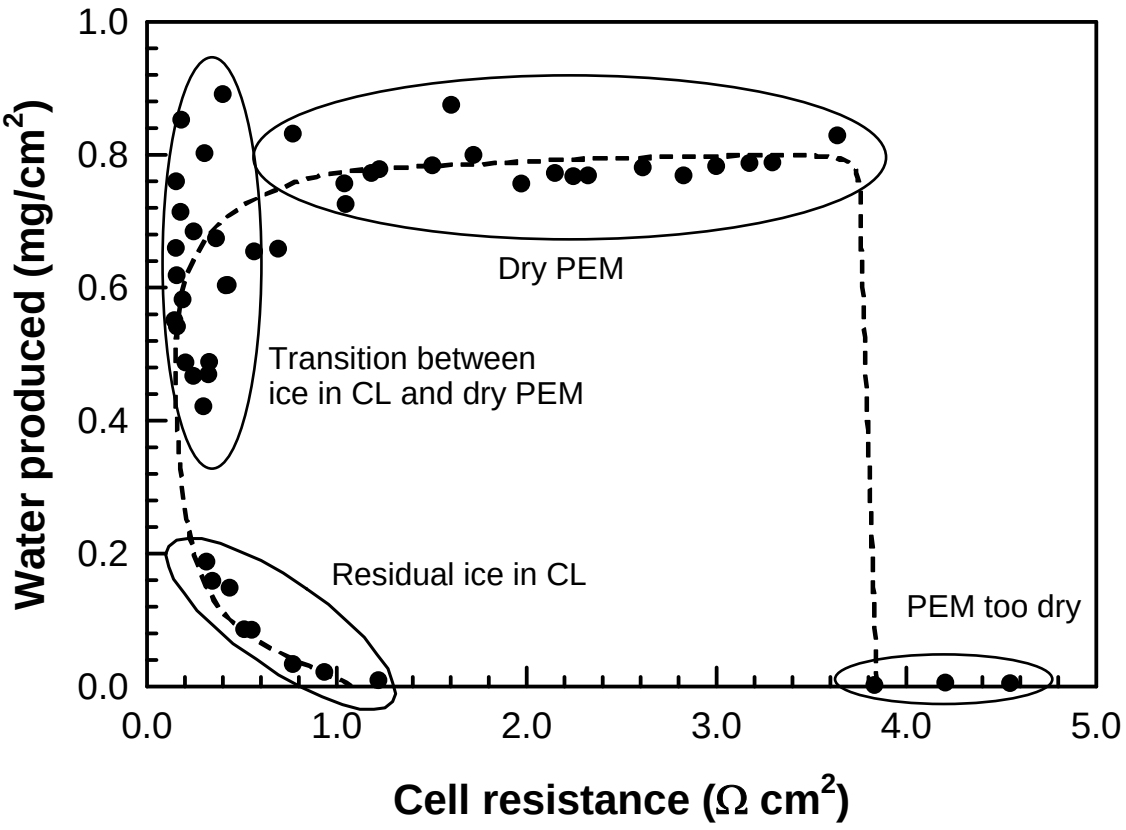

Figure 3.11 - Cold start performance as a function of cell resistance immediately prior to cold start, startup current density, i = 100 mA/cm^2. Each data point signifies a single cold start.

There are four different "zones" of resistance values in Figure 3.11, which can be related to Figure 3.6, that give significantly different cold start performance. The first zone, "Residual ice in CL", corresponds to "CL ice removal" in Figure 3.6, indicative of residual ice being present in the CL from the previous startup. This gives quite poor performance since the reaction sites of the CL are still partially covered or filled with ice. The second zone, "Transition between ice in CL and dry PEM", corresponds to the minimum value of resistance shown in Figure 3.6 and is representative of the transition between CL ice removal and membrane dehydration. This zone gives a large amount of scatter in performance since this transition is non-distinct; the processes of CL ice removal and membrane dehydration are in parallel. The "Dry PEM" corresponds to the "PEM dehydration" region seen in Figure 3.6 and gives the best and most predictable performance. This further reinforces the point that a dry membrane is beneficial for cold start. However, there is a region, "PEM too dry", where the membrane is too dry and therefore has a high resistivity which does not allow current to be drawn from the cell. The cut-off for this region is approximately 3.83 Ω cm^2 for this cell. In order to ensure a dry PEM and therefore optimal cold start performance for this cell tested, HFR prior to startup should range between 1.3 Ω cm^2 and 3.7 Ω cm^2.

The duality of values seen in Figure 3.11 is due to the path-dependent nature of cell resistance. Once again referencing Figure 3.6, a high resistance may be caused by CL ice or a dehydrated membrane. Understanding the cause of a specific cell resistance value is of vast importance and can be determined by the rate of change in resistance, denoted R'. Here the parameter R' is introduced, which utilizes the last two resistance

measurements prior to startup and quantifies the resistance change over time immediately prior to a cold start:

$$R' = \frac{dR}{dt} = \frac{\Delta R}{\Delta t} = \frac{R_2 - R_1}{t_2 - t_1} \tag{3.13}$$

A decrease in cell resistance, signified by a negative value of R', represents ice removal from the CL. An increase in cell resistance, signified by a positive value of R', represents membrane dehydration. A zero value of R' is representative of minimum resistance achievable which is the transition between CL ice removal and membrane dehydration. Figure 3.12 is a plot of the performance values associated with Figure 3.11 as a function of R'. The values in the region of "PEM too dry" are left out for clarity. As can be seen, a negative value of R' gives poor performance due to residual ice remaining in the CL. A zero value of R' gives a large amount of scatter, due to the non-distinct transition between CL ice removal and membrane dehydration. A positive value of R' gives optimal and repeatable cold start performance, which is a metric that can be used to ensure a positive startup in stacks.

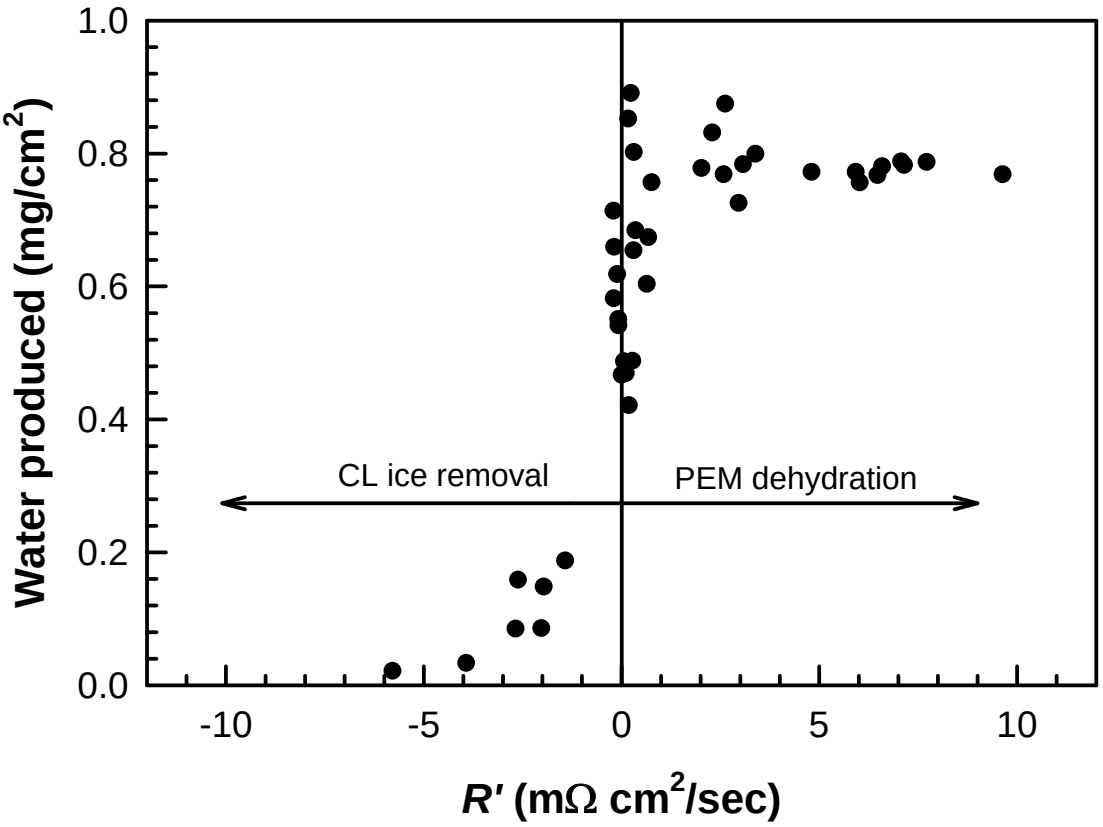

Figure 3.12 - Cold start performance as a function of *R'*, startup current density, *i* = 100 mA/cm^2. Each data point signifies a single cold start.

Chapter 4 Conclusions and Future Work

4.1 Conclusions

Cold starts were performed from -10°C in order to understand and diagnose the behavior of cell voltage and resistance. A new method of performing rapid and repeatable cold starts was introduced. The new method allows for successive cold starts to be performed without the necessity of reheating the cell, significantly reducing the time required for experimental cold starts. This method may also be employed to conduct extended cold start durability testing on a much quicker time scale than previous methods.

High frequency resistance has proven to be a key electrochemical diagnostic tool for cold start behavior and performance. Prior to cold start, cell resistance initially decreases due to CL ice removal then increases due to membrane dehydration. The parameter R' was introduced which measures the rate of change in cell resistance prior to startup. Optimal cold start performance occurs when R' is positive, indicating membrane dehydration. Negative values of R', indicative of residual ice remaining in the CL, give poor cold start performance.

During cold start, cell resistance initially decreases due to membrane hydration then increases due to CL ice formation. It was found that there is a maximum amount of water a dry membrane can absorb during startup before ice begins to form, regardless of current density. Based on this water absorption capability, the maximum change in

membrane water content was determined to be $(\Delta\lambda)_{max} \cong 6.4$. It was also found that lower startup current densities give a higher cell resistance at freeze-out. This higher final resistance is indicative of more ice being present in and around the CL at freeze-out. During freeze-out, lower startup current densities can produce more water than the cathode CL can theoretically store. This may be a sign of super-cooled liquid water diffusing out of the CL and freezing in the DM and CL|DM interface.

Using a lower startup current density gives better cold start performance in terms of total water, energy, and heat produced. However, lower startup current densities have slower production rates of each of these quantities. Regarding rapid stack startup, an optimal startup current density exits such that sufficient heat is generated to raise the stack above 0°C as quickly as possible.

4.2 Future Work

The method of consecutive cold starts introduced in the current work provides a novel experimental technique for performing rapid and repeatable experimental cold starts. Future work may be directed to improving this consecutive cold start procedure. For instance, varying the cold purge duration, flow rate, or gas may result in a more time efficient testing method. Another direction may be to use this procedure as a less time consuming method of determining the durability of various cell materials or designs undergoing numerous cold starts.

Since this aforementioned experimental technique can produce repeatable results, the effect of various cell materials or geometries on cold start performance may be studied. Various types of DM may be compared to determine each type's influence on CL insulation, product water storage, or damage mitigation. Several cell geometries may be also be studied to determine their effect on ice lens production, ice blockage, and general cold start performance.

A simulation that determined the effect of ice lens formation on HFR would be an interesting study. Some simulation cases may include the effective change in HFR depending on ice lens size, quantity, and location. The results of this simulation could then give guidelines for optimal flow field design in order to minimize degradation due to ice lens formation.

References

[1] M. M. Mench, "Fuel Cell Engines", *John Wiley & Sons Inc.*, New York, NY, 2008.

[2] X. Li, "Principles of Fuel Cells", *Taylor and Francis Group*, New York, NY, 2006.

[3] W. Vielstich, A. Lamm, H. A. Gasteiger, "Handbook of Fuel Cells", Vol 1, *John Wiley & Sons*, West Sussex, England, 2003.

[4] S. Um, C. Y. Wang, "Three-dimensional Analysis of Transport and Electrochemical Reactions in Polymer Electrolyte Fuel Cells", *Journal of Power Sources*, 125 (2004) 40-51.

[5] T. E. Springer, T. A. Zawodzinski, S. Gottesfeld, "Polymer Electrolyte Fuel Cell Model", *Journal of the Electrochemical Society*, Vol, 138, No. 8, (1991) 2334-2342.

[6] F. A. de Bruijn, in: T. S. Zhao, K-D. Kreuer, T. V. Nguyen, "Advances in Fuel Cells", Ch. 5, *Elsevier*, San Diego, CA, 2007, 235-336.

[7] K. R. Cooper, M. Smith, "Electrical test methods for on-line fuel cell ohmic resistance measurement", *Journal of Power Sources*, 160 (2006) 1088-1095.

[8] T. A. Zawodzinski, T. E. Springer, J. Davey, J. Valerio, S. Gottesfeld, "Water Transport Properties of Fuel Cell Ionomers", *The Electrochemical Society Proceedings of the Symposium on Modeling of Batteries and Fuel Cells*, (October 1991) 187-196.

[9] U. Beuscher, S. J. C. Cleghorn, W. B. Johnson, "Challenges for PEM fuel cell membranes", *International Journal of Energy Research*, 29 (2005) 1103-1112.

[10] K. Tajiri, Y. Tabuchi, C.Y. Wang, "Isothermal Cold Start of Polymer Electrolyte Fuel Cells", *Journal of the Electrochemical Society*, 154 (2007) B147-B152.

[11] M. Cappadonia, J. W. Erning, S. M. Saberi Niaki, U. Stimming, "Conductance of Nafion 117 membranes as a function of temperature and water content", *Solid State Ionics*, **77** (1995) 65-69.

[12] S. He, M. M. Mench, "One-Dimensional Transient Model for Frost Heave in Polymer Electrolyte Fuel Cells, I. Physical Model", *Journal of the Electrochemical Society*, 153 (2006) A1724-A1731.

[13] S. He, S. H. Kim, M. M. Mench, "1D Transient Model for Frost Heave in Polymer Electrolyte Fuel Cells, II. Parametric Study", *Journal of the Electrochemical Society*, 154 (2007) B1024-B1033.

[14] S. He, J. H. Lee, M. M. Mench, "1D Transient Model for Frost Heave in PEFCs, III. Heat Transfer, Microporous Layer, and Cycling Effects", *Journal of the Electrochemical Society*, 154 (2007) B1227-B1236.

[15] M. Oszcipok, D. Riemann, U. Kronenwett, M. Kreideweis, M. Zedda, "Statistic analysis of operational influences on the cold start behaviour of PEM fuel cells", *Journal of Power Sources*, 145 (2005) 407-415.

[16] M. Oszcipok, M. Zedda, D. Riemann, D. Geckeler, "Low temperature operation and influence parameters on the cold start ability of portable PEMFCs", *Journal of Power Sources*, 154 (2006) 404-411.

[17] K. Tajiri, Y. Tabuchi, F. Kagami, S. Takahashi, K. Yoshizawa, C.Y. Wang, "Effects of operating and design parameters on PEFC cold start", *Journal of Power Sources*, 165 (2007) 279-286.

[18] L. Mao, C.Y. Wang, "Analysis of Cold Start in Polymer Electrolyte Fuel Cells", *Journal of the Electrochemical Society*, 154 (2007) B139-B146.

[19] L. Mao, C.Y. Wang, Y. Tabuchi, "A Multiphase Model for Cold Start of Polymer Electrolyte Fuel Cells", *Journal of the Electrochemical Society,* 154 (2007) B341-B351.

[20] S. Ge, C.Y. Wang, "Characteristics of subzero startup and water/ice formation on the catalyst layer in a polymer electrolyte fuel cell", *Electrochimica Acta*, 52 (2007) 4825-4835.

[21] M. Khandelwal, S. Lee, M. M. Mench, "One-dimensional thermal model of cold-start in a polymer electrolyte fuel cell stack", *Journal of Power Sources*, 172 (2007) 816-830.

[22] Q. Yan, H. Toghiani, Y. W. Lee, K. Liang, H. Causey, "Effect of sub-freezing temperatures on a PEM fuel cell performance, startup and fuel cell components", *Journal of Power Sources*, 160 (2006) 1242-1250.

[23] S. Kim, M. M. Mench, "Physical degradation of membrane electrode assemblies undergoing freeze/thaw cycling: Microstructure effects", *Journal of Power Sources*, 174 (2007) 206-220.

[24] S. Kim, B. K. Ahn, M. M. Mench, "Physical degradation of membrane electrode assemblies undergoing freeze/thaw cycling: Diffusion media effects" *J. Power Sources*, 179 (2008) 140-146.

[25] Y. Hishinuma, T. Chikashisa, F. Kagami, T. Ogawa, "The Design and Performance of a PEFC at a Temperature Below Freezing", *JSME International Journal*, B 47 (2004) 234-241.

[26] Y. Ishikawa, T. Morita, K. Nakata, K. Yoshida, M. Shiozawa, "Verification of generated water in a super-cooled state below freezing point in PEFC", *Electrochemical Society Transactions*, 1 (2005) 359-364.

[27] Y. Ishikawa, T. Morita, K. Nakata, K. Yoshida, M. Shiozawa, "Behavior of water below the freezing point in PEFCs", *Journal of Power Sources*, 163 (2007) 708-712.

[28] S. Ge, C.Y. Wang, "In Situ Imaging of Liquid Water and Ice formation in an Operating PEFC during Cold Start", *Electrochemical and Solid-State Letters*, 9 (2006) A499-A503.

[29] M. Oszcipok, A. Hakenjos, D. Riemann, C. Hebling, "Startup and Freezing Processes in PEM Fuel Cells", *Fuel Cells*, 2 (2007) 135-141.

[30] F. Jiang, W. Fang, C.Y. Wang, "Non-isothermal cold start of polymer electrolyte fuel cells", *Electrochim. Acta*, 53 (2007) 610-621.